

See discussions, stats, and author profiles for this publication at: <https://www.researchgate.net/publication/259508294>

# Discretization error for the Discrete Kirchhoff plate finite element approximation

Article in *Computer Methods in Applied Mechanics and Engineering* · February 2014

DOI: 10.1016/j.cma.2013.11.011

---

CITATIONS

2

---

READS

115

3 authors, including:



Uroš Bohinc

Zavod za gradbeništvo Slovenije

7 PUBLICATIONS 12 CITATIONS

SEE PROFILE



Boštjan Brank

University of Ljubljana

61 PUBLICATIONS 612 CITATIONS

SEE PROFILE

# *Discretization error for the Discrete Kirchhoff plate finite element approximation*

Uroš Bohinc<sup>1</sup>, Boštjan Brank<sup>2</sup> and Adnan Ibrahimbegovic<sup>3</sup>

<sup>1</sup> Slovenian Nat. Building and Civil Eng. Institute, Ljubljana, Slovenia

<sup>2</sup> University of Ljubljana, FGG, Slovenia

<sup>3</sup> Ecole Normale Supérieure, LMT-Cachan, France

## **Abstract:**

We provide in this work the discretization error estimates that can guide an adaptive mesh refinement for the Discrete Kirchhoff plate finite elements. The proposed developments are built upon the concept of error estimates for classical elasticity and adapted to suit the Kirchhoff plate finite elements. We give a detailed illustration of the proposed procedures for the discrete Kirchhoff triangular plate element, along with several different possibilities for constructing the enhancement of test space needed for error estimates. The first novelty concerns the consistent displacement field in terms of the third order polynomial for the Discrete Kirchhoff triangle, whereas the second novelty is the use of Argyris triangle with fifth order polynomials for constructing the enhanced test for error estimates. We compare the latter against several alternatives that can be used for Kirchhoff plates. The results of numerical examples are given to illustrate the effectiveness of proposed discretization error estimates.

Keywords: Kirchhoff plates, Discrete Kirchhoff Triangle, finite element, discretization error

# 1 Introduction

There exist numerous applications in aerospace, civil and mechanical engineering, which call for the thin plate finite element (FE) modelling. Thus the problem we address in this work pertaining to the finite element discretization errors that can guide an optimal mesh choice with respect to a required level of solution accuracy, is certainly of large practical interest. This is further reinforced by the main focus of our work upon frequently used plate finite elements, referred to as the Discrete Kirchhoff (DK) elements (e.g. [8], [7], [11]). These elements are widely popular for their capabilities to deliver higher-order approximations for thin plate structures, even for finite elements with small number of nodes. The plate elements of this kind are part of many commercial FE codes, either as 3-node triangle (DKT) or as 4-node quadrilateral (DKQ).

The DK elements are the result of a long line of developments on Kirchhoff plate elements requiring  $C^1$  continuity of transverse displacement interpolation. Early development using cubic polynomials were only partially successful, since they resulted with very complex interpolation schemes, not easy to generalize to any other than particular triangular in [20] or quadrilateral element in [19]. Only partial success was also met by interpolation scheme for Kirchhoff plates in form of the complete fifth-order polynomial proposed for triangular element [4]. Such an interpolation employs the nodal interpolation parameters that include not only displacements and rotations (or the first derivatives), but also the curvatures (or the second derivatives). The curvatures as kinematic nodal unknowns can happen to be in disagreement with the curvatures computed from the constitutive equations for bending-moments; one such example pertains to setting these curvatures to zero in corner points of the skew plate with Neumann boundary, which can cause element to lock. For these reasons, the Kirchhoff plate elements were abandoned and preference was given to Reissner-Mindlin (RM) thick plate elements, using only  $C^0$  interpolations for displacement and independent rotations. The interpolations of this kind are very easy to generate for different numbers of element nodes; however, they reduce the order of approximation with respect to Kirchhoff plate elements with the same number of nodes. More importantly, the Reissner-Mindlin plate elements turned to be very sensitive to shear locking phenomena (for summary of a vast number of remedies, see [39] or [24]).

The DK elements was introduced within the RM plate theory framework, trying to deal with shear locking by completely removing the shear deformation. This was done by using simple linear interpolations for both displacement and rotations, tying them by imposing the Kirchhoff constraint at each element edge (e.g. [8], [7], [11]). The fully consistent mixed formulation of DKQ plate elements is proposed in [26], along with a non-conventional displacement field interpolation in terms of cubic polynomial. The same approach is extended here to DKT plate elements. It was shown in [25] that the same mixed variational framework and modified non-conventional interpolations, properly enhanced with incompatible modes, can be used to develop a thick plate equivalent to DKQ plate element, which also provides bi-linear approximation for bending

moments in 4-node element. The latter was exploited in [12] to construct the plate model adaptivity procedure, which can effectively indicate the elements for which the shear energy is not negligible. The recent works on theoretical foundation of Kirchhoff or Reissner-Mindlin plate theories (e.g. [3], [13]) also make use of this kind of mixed variational formulation in order to provide the plate models justification with respect to three-dimensional elasticity. We note in passing that these results, which showed the importance of taking into account a quadratic variation in transverse displacement in through-the-thickness direction, can eventually be used to complete the model adaptivity procedure [12] with estimates pertinent to the change of thickness. These results are also in agreement with our previous works on geometrically nonlinear shell models featuring the same quadratic variation in through-the-thickness direction that can accommodate directly 3D constitutive laws (e.g. [15]).

However, the best choice of the finite element discretization with DK plate elements has not yet been fully understood, and there persists the need for providing the error estimates for guiding the mesh refinement. That is the main goal of this work.

The discretization by FE method provides an approximate solution to a given boundary value problem ([39], [27]). Estimates of the discretization error of the FE solution are of interest for the adaptive mesh refinement (e.g. [2], [30], [35]). The results on discretization error estimates for biharmonic operator typical of Kirchhoff plates are available (e.g. see [18]) only for the conventional Kirchhoff elements [20] or [4], which are hardly used nowadays. Only limited success is provided for non-conventional Kirchhoff plate elements, for the simplest choice with constant approximation in each element known as Morley triangle (e.g. [21], [23], [32]). For a more refined plate element with non-conventional interpolations like Discrete Kirchhoff, the most appropriate error estimates are still to be established.

In constructing FE discretization error estimates, the preference is given to a posteriori version that starts from the computed solution of the FE produced set of equilibrium equations; one can consider two types of methods (e.g. [30]): i) explicit estimates that bound the displacement discretization error with an unknown global constant times the norm of residual of equilibrium equations (e.g. [6]); or ii) implicit estimates that rely upon the subsequent post-processing of the FE solution in order to obtain the enhanced displacement and stress of increased accuracy and thus provide the corresponding error estimates by comparison against FE solution, with no need for constants. The latter is the favourite choice for solid mechanics problems, with the two main types of procedures for constructing enhanced solution by using either the superconvergent patch recovery (SPR) or the equilibrated boundary stress resultants (EqR). The SPR enhanced solution (e.g. see [40], [38]) is the least square best fit by a smooth stress interpolation of the FE results computed in superconvergence points (roughly, the reduced numerical integration points of a particular element). The same implementation is kept for both continuum and DK plate elements, with either stresses or bending moments being processed, one component at the time. The EqR enhanced solution (e.g. see [29], [2], [30], [35], [9])

makes use of the equilibrated element boundary traction. Such a solution can be obtained with higher-order FE approximations to provide the solution to a local Neumann boundary value problems in each single element (e.g. [36], [17], [1]).

The main thrust in this work is directed towards the direct application of the EqR procedure for constructing a posteriori error estimates for the Discrete Kirchhoff plate elements. The SPR procedure is used only for comparison, showing that its performance need not always be optimal for the elements with higher order interpolations, such as Discrete Kirchhoff plate element. The first novelty concerns explicit definition of the finite element interpolation with cubic displacement field for the the Discrete Kirchhoff Triangular (DKT) element. We also adapt to DKT element the EqR approach that was initially derived for solid mechanics finite elements with only  $\mathcal{C}^0$  interpolations. Among several alternatives for constructing the enhanced test space, the main novelty concerns using the conforming Kirchhoff plate element of [4], which has not been often used by engineering community for it requires imposing the nodal values of curvatures.

The outline of the paper is as follows. In Section 2, we briefly summarize the governing equations of the Kirchhoff plate theory, its strong and weak forms. In Section 3, we present two triangular Kirchhoff plate finite elements employed as the main ingredients of the proposed approach, the Discrete Kirchhoff and Argyris. All the governing equations of residual based local and global error indicators are given in Section 4. In Section 5, we provide the details of implementation of EqR method for the DKT plate elements. Numerical examples are presented in Section 6. The concluding remarks are given in Section 7.

## 2 Kirchhoff plate bending model

The main governing equations of the Kirchhoff plate model are summarized here (for details, see e.g. [34]), in order to define the solid theoretical basis for the developments to follow.

### 2.1 Model main ingredients

Consider an elastic plate, whose middle-plane is placed in  $xy$  plane and occupying the domain  $\Omega$ , the middle-plane boundary  $\Gamma_p = \Gamma_N \cup \Gamma_D$ ,  $\Gamma_N \cap \Gamma_D = \emptyset$ , and the plate thickness  $t$ ,  $[\frac{-t}{2}, \frac{t}{2}] \ni z$ . At a boundary point, two vectors are defined:  $\mathbf{s} = [-n_y, n_x]^T$ , and  $\mathbf{n} = [n_x, n_y]^T$ , where  $\mathbf{n}$  is the outward unit exterior normal at the plate boundary. Coordinates  $s$  and  $n$  change, respectively, along the boundary and in the direction of the normal. The plate is loaded by distributed area loading  $f : \Omega \rightarrow \mathbb{R}$ , line boundary moment in  $s$  direction  $\overline{m}_s : \Gamma_N \rightarrow \mathbb{R}$  and line boundary force in  $z$  direction specifying the effective shear  $\bar{q}_{ef} : \Gamma_N \rightarrow \mathbb{R}$  (see (10)).

The Kirchhoff plate model is built upon the main kinematic constraint of through-the-thickness fibre that remains perpendicular to the plate middle sur-

face, which allows to define the fibre rotations  $\boldsymbol{\theta} = [\theta_x, \theta_y]^T$  as the derivatives of the plate transverse displacement  $w : \Omega \cup \Gamma_p \rightarrow \mathbb{R}$ :

$$\nabla^K w - \boldsymbol{\theta} = \mathbf{0}, \quad \nabla^K = \left[ \frac{\partial}{\partial y}, -\frac{\partial}{\partial x} \right]^T \quad (1)$$

The above constraint sets the transverse shear strains to zero. Thus, the only generalized deformations are middle-plane curvatures  $\boldsymbol{\kappa} = [\kappa_{xx}, \kappa_{yy}, 2\kappa_{xy}]^T$ , defined as the second derivatives of  $w$

$$\kappa_{xx} = \frac{\partial^2 w}{\partial x^2} = -\frac{\partial \theta_y}{\partial x}, \quad \kappa_{yy} = \frac{\partial^2 w}{\partial y^2} = \frac{\partial \theta_x}{\partial y}, \quad \kappa_{xy} = \frac{\partial^2 w}{\partial x \partial y} = \left( \frac{\partial \theta_x}{\partial x} - \frac{\partial \theta_y}{\partial y} \right) / 2 \quad (2)$$

The curvatures relate to the bending moments  $\mathbf{m} = [m_{xx}, m_{yy}, m_{xy}]^T$  through stress-resultant constitutive equations:

$$\mathbf{m} = D \underbrace{\left[ \begin{bmatrix} 1 & \nu & 0 \end{bmatrix}^T, \begin{bmatrix} \nu & 1 & 0 \end{bmatrix}^T, \begin{bmatrix} 0 & 0 & \frac{1-\nu}{2} \end{bmatrix}^T \right]}_{\mathbf{C}_B} \boldsymbol{\kappa}; \quad D = \frac{Et^3}{12(1-\nu^2)} \quad (3)$$

where  $E$  is Young's modulus and  $\nu$  is Poisson's ratio. According to the Kirchhoff hypothesis and the corresponding zero value of shear strains, there cannot be similar role for shear constitutive equations. Rather, the shear forces have to be computed directly from corresponding moment equilibrium equations with

$$q_x = -\left( \frac{\partial m_{xx}}{\partial x} + \frac{\partial m_{xy}}{\partial y} \right), \quad q_y = -\left( \frac{\partial m_{yy}}{\partial y} + \frac{\partial m_{xy}}{\partial x} \right) \quad (4)$$

The last two results can be inserted into force equilibrium equation, in order to provide a single equilibrium equation in terms of moments as

$$\frac{\partial q_x}{\partial x} + \frac{\partial q_y}{\partial y} + f = 0 \implies \frac{\partial m_{xx}^2}{\partial x^2} + 2 \frac{\partial^2 m_{xy}}{\partial x \partial y} + \frac{\partial m_{yy}^2}{\partial y^2} = f \quad (5)$$

The following transformations applied at the plate boundary allow us to define the boundary rotations

$$\theta_n = \frac{\partial w}{\partial s} = \underbrace{-n_y \frac{\partial w}{\partial x}}_{-\theta_y} + \underbrace{n_x \frac{\partial w}{\partial y}}_{\theta_x}, \quad -\theta_s = \frac{\partial w}{\partial n} = \underbrace{n_x \frac{\partial w}{\partial x}}_{-\theta_y} + \underbrace{n_y \frac{\partial w}{\partial y}}_{\theta_x} \quad (6)$$

along with the boundary moment components

$$m_{nn} = n_x^2 m_{xx} + n_y^2 m_{yy} + 2n_x n_y m_{xy} \quad (7)$$

$$m_{ns} = -n_x n_y m_{xx} + n_x n_y m_{yy} + (n_x^2 - n_y^2) m_{xy} \quad (8)$$

and the boundary shear forces

$$q_n = n_x q_x + n_y q_y = -\left( \frac{\partial m_{nn}}{\partial n} + \frac{\partial m_{ns}}{\partial s} \right) \quad (9)$$

The Kirchhoff hypothesis imposes the effective shear force, combining the shear with twisting moments derivative along the mid-plane boundary, as the only appropriate way for imposing the Neumann boundary conditions

$$q_{ef} = q_n - \frac{\partial m_{ns}}{\partial s} \text{ on } \Gamma_P, \quad \bar{q}_{ef} = \bar{q} - \frac{\partial \bar{m}_{ns}}{\partial s} \text{ on } \Gamma_N \quad (10)$$

In general, the boundary can be split into the Neumann  $\Gamma_N$ , where we impose the normal moment and effective shear force  $(\bar{m}_{nn}, \bar{q}_{ef})$ , and the Dirichlet  $\Gamma_D$ , where we impose displacement and its normal derivative  $\bar{w}, \frac{\partial \bar{w}}{\partial n}$ . We can also have a mixed case or Navier boundary  $\Gamma_M$ , where we impose the displacement and normal moment  $\bar{w}, \bar{m}_{nn}$ .

## 2.2 Strong and weak forms

By combining the above defined kinematic, constitutive, and equilibrium equations into a single equation, we define the strong form of the boundary value problem for the Kirchhoff plate. It can be stated as:

Given: distributed load  $f$  in  $\Omega$ , imposed boundary shear and moments  $\bar{q}_{ef}$ ,  $\bar{m}_s$  and imposed displacement and rotation  $\bar{w}, \bar{\theta}_s$

Find:  $w$ , such that

$$\begin{aligned} \Delta \Delta w &= f/D ; \Delta = \frac{\partial^2}{\partial x^2} + \frac{\partial^2}{\partial y^2} \text{ in } \Omega \\ w &= \bar{w} ; -\frac{\partial w}{\partial n} = \bar{\theta}_s ; \text{ on } \Gamma_D \\ w &= \bar{w} ; m_{nn}(w) = -\bar{m}_s \text{ on } \Gamma_M \\ q_{ef}(w) &= \bar{q}_{ef} ; m_{nn}(w) = -\bar{m}_s \text{ on } \Gamma_N \end{aligned} \quad (11)$$

We note in passing that for any corner point  $P$  on  $\Gamma_N$ ,  $-m_{ns}|_{P-} + m_{ns}|_{P+} = -\bar{m}_n|_{P-} + \bar{m}_n|_{P+}$ .

The corresponding variational formulation, considering the weak form of plate equilibrium equation along with strong form of kinematics and constitutive equations, can be written as

$$a(w, v) = l(v), \quad w \in \mathcal{V}, \quad \forall v \in \mathcal{V}_0 \quad (12)$$

where

$$a(w, v) = \int_{\Omega} \boldsymbol{\kappa}^T(v) \mathbf{C}_B \boldsymbol{\kappa}(w) \, d\Omega \quad (13)$$

$$l(v) = \int_{\Omega} v f \, d\Omega + \sum_{\Gamma_{IJ}} \left( \int_{\Gamma_{IJ}} (v \bar{q}_{ef} + \theta_s \bar{m}_s) \, ds + [v \bar{m}_n]_I^J \right) \quad (14)$$

Here,  $I, J \in G_N$ ,  $\Gamma_{IJ} \subset \Gamma_N$ , and  $\sum_{\Gamma_{IJ}} = \Gamma_N$  is the counter-clockwise sum of boundary sections. The trial and the test spaces in (12) are defined as:

$$\mathcal{V} = \left\{ w \in \mathcal{H}^2(\Omega) \mid w = \bar{w}, -\frac{\partial w}{\partial n} = \bar{\theta}_s \text{ on } \Gamma_D \mid w = \bar{w} \text{ on } \Gamma_M \right\} \quad (15)$$

$$\mathcal{V}_0 = \left\{ v \in \mathcal{H}^2(\Omega) \mid v = 0, -\frac{\partial v}{\partial n} = \theta_s = 0 \text{ on } \Gamma_D \mid v = 0 \text{ on } \Gamma_M \right\} \quad (16)$$





Kirchhoff plate problem lies in the fact that the natural variational space (15) for the biharmonic strong form is the second order Sobolev space  $\mathcal{H}^2$ . Thus,  $\mathcal{C}^1$ -continuity is imposed on  $w_h$ , which requires higher-order polynomials over FE domain  $\Omega_{h,e} \subset \Omega_h$ . The plate element of Argyris [4] delivers this kind of approximation, but it uses the second derivatives of displacement or curvatures. In order to overcome this difficulty for lower-order polynomials, non-standard FE approximations for Discrete Kirchhoff are needed, but they no longer provide continuous moments across element boundaries.

### 3.1 Conforming Kirchhoff triangle of Argyris

The starting point in development of the discrete approximation is the displacement-type weak form in (12) requiring  $\mathcal{C}^1$  continuity of displacement field. This can be achieved by using the conforming Kirchhoff triangle of [4] with discrete approximation of displacement field  $w_{h,e} = w_{h|e}$  in terms of complete 5<sup>th</sup> order polynomial. The latter counts 21 terms, and thus the Argyris element has 21 degrees of freedom, counting among them (see Figure 2 for illustration):  $w_I, w_{I,x}, w_{I,y}, w_{I,xx}, w_{I,yy}, w_{I,xy}$  at any vertex node ( $I = 1, 2, 3$ ), and  $w_{J,n}$  at mid-side node ( $J = 4, 5, 6$ ). The trial and the test subspaces for such plate finite elements can be written as:

$$\mathcal{V}_h^{ARG} = \{w_h \in \mathcal{V} \mid w_{h|e} \in P_5(e) \quad \forall e \in \mathcal{C}_h\} \quad (20)$$

$$\mathcal{V}_{0,h}^{ARG} = \{v_h \in \mathcal{V}_0 \mid v_{h|e} \in P_5(e) \quad \forall e \in \mathcal{C}_h\} \quad (21)$$

where  $P_5(e)$  is the space of polynomials of degree at most 5 on triangle  $e$ , and  $\mathcal{C}_h$  represents the collection of all the elements of the mesh.

The approximation of the displacement field is  $w_{h,e}(\zeta) = \boldsymbol{\omega}(\zeta)\mathbf{p}$ , where  $\zeta = [\zeta_1, \zeta_2, \zeta_3]$  are area coordinates ( $\sum_{I=1}^3 \zeta_I = 1$ ), [39],  $\mathbf{p}$  is vector of 21 non-zero constants, and  $\boldsymbol{\omega}$  is transposed vector of 21 polynomials that define complete 2-dimensional quintic interpolation. Those polynomials can be given as [4]

$$\begin{aligned} \boldsymbol{\omega} = & [\zeta_1^5, \zeta_2^5, \zeta_3^5, \\ & \zeta_1\zeta_2^4, \zeta_2\zeta_3^4, \zeta_3\zeta_1^4, \zeta_2\zeta_1^4, \zeta_3\zeta_2^4, \zeta_1\zeta_3^4, \\ & \zeta_1^3\zeta_2^2, \zeta_2^3\zeta_3^2, \zeta_3^3\zeta_1^2, \zeta_2^3\zeta_1^2, \zeta_3^3\zeta_2^2, \zeta_1^3\zeta_3^2, \\ & \zeta_1^3\zeta_2\zeta_3, \zeta_1\zeta_2^3\zeta_3, \zeta_1\zeta_2\zeta_3^3, \zeta_1^2\zeta_2^2\zeta_3, \zeta_1^2\zeta_2\zeta_3^2, \zeta_1\zeta_2^2\zeta_3^2] \end{aligned} \quad (22)$$

The constants  $\mathbf{p}$  relate to the natural degrees of freedom of the element  $\mathbf{w}_\rho$

$$\begin{aligned} \mathbf{w}_\rho = & [w_1, w_{1,12}, w_{1,31}, w_{1,12^2}, w_{1,31^2}, w_{1,23^2}, \\ & w_2, w_{2,23}, w_{2,12}, w_{2,12^2}, w_{2,31^2}, w_{2,23^2}, \\ & w_3, w_{3,31}, w_{3,23}, w_{3,12^2}, w_{3,31^2}, w_{3,23^2}, \\ & w_{1-2,n}, w_{2-3,n}, w_{3-1,n}]^T \end{aligned} \quad (23)$$

as  $\mathbf{p} = \mathbf{A}\mathbf{w}_\rho$ . In  $\mathbf{w}_\rho$ , the derivatives are formed with respect to the natural coordinates. Hence,  $w_{K,IJ}$  is derivative of  $w_{h,e}$  with respect to  $s_{IJ} \in [0, L_{IJ}]$

that runs from vertex node  $I$  towards vertex node  $J$  ( $L_{IJ}$  is the length of that edge), evaluated at vertex node  $K$ . Similarly,  $w_{K,IJ^2}$  is 2<sup>nd</sup> the derivative of  $w_{h,e}$  with respect to that parameter, evaluated at vertex node  $K$ . The above derivatives are given as ([4])

$$w_{h,e,IJ} = \frac{\partial w_{h,e}}{\partial \zeta_J} - \frac{\partial w_{h,e}}{\partial \zeta_I}, \quad w_{h,e,IJ^2} = \frac{\partial^2 w_{h,e}}{\partial \zeta_J^2} - 2 \frac{\partial w_{h,e}}{\partial \zeta_I} \frac{\partial w_{h,e}}{\partial \zeta_J} + \frac{\partial^2 w_{h,e}}{\partial \zeta_I^2} \quad (24)$$

Furthermore,  $w_{I-J,n}$  in (23) denotes derivative of  $w_{h,e}$  with respect to the normal to the edge (defined by vertex nodes  $I$  and  $J$ ) evaluated at the mid-side node

$$w_{I-J,n} = \left[ 2 \frac{\partial w_{h,e}}{\partial \zeta_K} - \left( \frac{\partial w_{h,e}}{\partial \zeta_I} + \frac{\partial w_{h,e}}{\partial \zeta_J} \right) + \mu_{IJ} \left( \frac{\partial w_{h,e}}{\partial \zeta_J} - \frac{\partial w_{h,e}}{\partial \zeta_I} \right) \right]_{|\zeta_{I-J}} \quad (25)$$

vertex nodes notation	1 - 2	2 - 3	3 - 1
mid-side node notation, Fig. 2	4	5	6

Here,  $K \neq I \neq J$  is the 3<sup>rd</sup> vertex node,  $\mu_{IJ} = 2\mathbf{x}_{IJ}^T (\mathbf{x}_K - (\mathbf{x}_I + \mathbf{x}_J)/2) / L_{IJ}^2$ ,  $\mathbf{x}_{IJ} = \mathbf{x}_J - \mathbf{x}_I$ ,  $\mathbf{x}_K = [x_K, y_K]^T$ , and  $\zeta_{I-J}$  is value of  $\zeta$  at the mid-side node. The matrix  $\mathbf{A}$  (of constant entries) can be obtained by evaluating  $w_{h,e}(\zeta) = \boldsymbol{\omega}(\zeta)\mathbf{p}$  and derivatives (24) at vertex nodes, and (25) at mid-side nodes

Node	1	2	3	4	5	6
$\zeta$	[1, 0, 0]	[0, 1, 0]	[0, 0, 1]	[ $\frac{1}{2}, \frac{1}{2}, 0$ ]	[ $0, \frac{1}{2}, \frac{1}{2}$ ]	[ $\frac{1}{2}, 0, \frac{1}{2}$ ]

(26)

and equating the results to  $\mathbf{w}_\rho$ . Once  $\mathbf{A}$  is known, one can transform nodal  $\zeta$ -derivatives to nodal  $x, y$ -derivatives. The following transformations are valid for any point of the triangle (see [4]):

$$\begin{bmatrix} w_{h,e,12} \\ w_{h,e,23} \\ w_{h,e,31} \end{bmatrix} = \begin{bmatrix} x_{12} & y_{12} \\ x_{23} & y_{23} \\ x_{31} & y_{31} \end{bmatrix} \begin{bmatrix} w_{h,e,x} \\ w_{h,e,y} \end{bmatrix} \quad (27)$$

$$\underbrace{\begin{bmatrix} w_{h,e,12^2} \\ w_{h,e,23^2} \\ w_{h,e,31^2} \end{bmatrix}}_{\kappa_\rho} = \underbrace{\begin{bmatrix} x_{12}^2 & y_{12}^2 & x_{12}y_{12} \\ x_{23}^2 & y_{23}^2 & x_{23}y_{23} \\ x_{31}^2 & y_{31}^2 & x_{31}y_{31} \end{bmatrix}}_{\mathbf{T}^{-1}} \underbrace{\begin{bmatrix} w_{h,e,xx} \\ w_{h,e,yy} \\ 2w_{h,e,xy} \end{bmatrix}}_{\kappa_h} \quad (28)$$

where  $x_{IJ} = x_J - x_I$  and  $y_{IJ} = y_J - y_I$ . With the transformations (27) and (28) in hand, one can form relation  $\mathbf{w}_\rho = \mathbf{X}_T \bar{\mathbf{u}}^e$ , where  $\bar{\mathbf{u}}^e$  are element degrees of freedom from Fig. 2

$$\bar{\mathbf{u}}^e = [w_1, w_{1,x}, w_{1,y}, w_{1,xx}, w_{1,xy}, w_{1,yy}, w_2, w_{2,x}, w_{2,y}, w_{2,xx}, w_{2,xy}, w_{2,yy}, w_3, w_{3,x}, w_{3,y}, w_{3,xx}, w_{3,xy}, w_{3,yy}, w_{1-2,n}, w_{2-3,n}, w_{3-1,n}]^T \quad (29)$$

and  $\mathbf{X}_T$  is matrix of constant entries. It follows from the above that  $w_{h,e}(\zeta) = \boldsymbol{\omega}(\zeta) \mathbf{A} \mathbf{X}_T \bar{\mathbf{u}}^e$ , where  $\boldsymbol{\omega}(\zeta) \mathbf{A} \mathbf{X}_T = \boldsymbol{\omega}(\zeta) \mathbf{X}$  is transposed vector of shape functions. The approximation of curvature vector  $\boldsymbol{\kappa}_h$  is, see (28)

$$\boldsymbol{\kappa}_h = \mathbf{T} \boldsymbol{\kappa}_\rho = \mathbf{T} \underbrace{\begin{bmatrix} \omega_{,12^2} \\ \omega_{,23^2} \\ \omega_{,31^2} \end{bmatrix}}_{\bar{\boldsymbol{\omega}}_\rho} \underbrace{\mathbf{A} \mathbf{X}_T}_{\mathbf{X}} \bar{\mathbf{u}}^e = \underbrace{\mathbf{T} \bar{\boldsymbol{\omega}}_\rho}_{\boldsymbol{\omega}_\rho} \mathbf{X} \bar{\mathbf{u}}^e \quad (30)$$

where  $\omega_{,IJ^2}$  is obtained as, see (24),  $\omega_{,IJ^2} = \frac{\partial \omega^2}{\partial \zeta_J^2} - 2 \frac{\partial \omega}{\partial \zeta_I} \frac{\partial \omega}{\partial \zeta_J} + \frac{\partial \omega^2}{\partial \zeta_I^2}$ .

The same type interpolation as defined for trial functions  $w_{h,e}$  is also used for test functions  $v_{h,e}$ , with appropriate nodal values  $\bar{\mathbf{v}}^e$  and corresponding constraint of kinematic admissibility. By further replacing these interpolations into the bilinear form in (12), we can obtain the element stiffness matrix  $\mathbf{K}^e$ :

$$\begin{aligned} a(w_{h,e}, v_{h,e}) &= \int_{\Omega_{e,h}} \boldsymbol{\kappa}_h^T(v_{h,e}) \mathbf{m}_h(w_{h,e}) d\Omega = \int_{\Omega_{e,h}} \boldsymbol{\kappa}_\rho^T(v_{h,e}) \mathbf{G} \boldsymbol{\kappa}_\rho(w_{h,e}) d\Omega \\ &= \bar{\mathbf{v}}^{e,T} \int_{\Omega_{e,h}} \boldsymbol{\omega}_\rho^T \mathbf{G} \boldsymbol{\omega}_\rho d\Omega \bar{\mathbf{u}}^e = \bar{\mathbf{v}}^{e,T} \mathbf{K}^e \bar{\mathbf{u}}^e \end{aligned} \quad (31)$$

where  $\mathbf{G} = \mathbf{T}^T \mathbf{C}_B \mathbf{T}$ . The last integral in (31) is obtained by analytical integration. The element load vector follows from using the above interpolation in the linear form (31)

$$\begin{aligned} l(v_{h,e}) &= \bar{\mathbf{v}}^{e,T} \mathbf{X}^T \left[ \int_{\Omega_{e,h}} \boldsymbol{\omega}^T f d\Omega + \sum_{\Gamma_{IJ}} \left( \int_{\Gamma_{IJ}} (\boldsymbol{\omega}^T \bar{q}_{ef} - \boldsymbol{\omega}_{,n}^T \bar{m}_s) ds + [\boldsymbol{\omega}^T \bar{m}_n]_I^J \right) \right] \\ &= \bar{\mathbf{v}}^{e,T} \mathbf{f}^e \end{aligned} \quad (32)$$

where  $\boldsymbol{\omega}_{,n} = \frac{\partial \boldsymbol{\omega}}{\partial n}|_{\Gamma_{IJ}} = 2 \frac{\partial \boldsymbol{\omega}}{\partial \zeta_K} - \left( \frac{\partial \boldsymbol{\omega}}{\partial \zeta_I} + \frac{\partial \boldsymbol{\omega}}{\partial \zeta_J} \right) + \mu_{IJ} \left( \frac{\partial \boldsymbol{\omega}}{\partial \zeta_J} - \frac{\partial \boldsymbol{\omega}}{\partial \zeta_I} \right)$ , see (25). The integrals in (32) are obtained in closed form. All other details for this element are given in [4].

The Kirchhoff triangular plate element of Argyris ensures the continuity of bending moments across the element boundaries. Under such conditions, one can provide the error estimates and confirm the convergence for the plate discretization of this kind (e.g. see [18], p. 296), resulting with the error estimate for  $k - th$  order polynomial approximations that reads:

$$\|w - w_h\|_{2,\Omega} \leq C h^{k-1} |w|_{k+1,\Omega} \quad (33)$$

where  $C$  is a constant independent of characteristic element size  $h$ . In other words, for the regular solution  $w \in H^6(\Omega)$ , the error norm in displacement field computed by the Argyris element is of  $O(h^4)$ . The Argyris element provides the continuity of moments, which is also the key requirement for rigorous error estimates (e.g. see [16] or [5]). However, the continuity of moments also enforces continuity of curvatures, which requires to impose the curvature nodal values. The

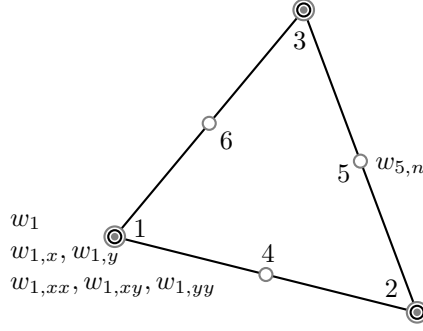


Figure 2: Degrees of freedom of Argyris plate triangular element

latter turned into the main weakness of the Argyris element that kept it from becoming the standard engineering tool for plates, and the Discrete Kirchhoff element finally became the favourite. However, the Argyris plate can perfectly serve in tandem with the DKT plate element for constructing discretization error estimates by solving the local Neumann problems, as explained in the next section.

### 3.2 Discrete Kirchhoff triangle

In order to explain how non-standard DKT interpolations are designed, we can start with the mixed variational formulation (e.g. [28]), replacing the formulation for Kirchhoff plate in (17). The main goal is to reduce the displacement continuity requirements by introducing an independent shear strain field  $\gamma$ , along with the corresponding weak form of the Kirchhoff hypothesis. We can write this mixed variational formulation:

$$\begin{aligned} a_\gamma(\mathbf{u}, \gamma, \mathbf{q}; \mathbf{v}) &= l(\mathbf{v}) ; \quad a_\gamma(\mathbf{u}, \gamma; \mathbf{v}) = \int_\Omega \{ \boldsymbol{\kappa}^T(\mathbf{v}) \mathbf{m}(\mathbf{u}) + [\gamma(\mathbf{v}) - \gamma^*]^T \mathbf{q} \} d\Omega \\ \int_\Omega \{ \mathbf{q}^{*,T} [\gamma(\mathbf{u}) - \gamma]^T \} d\Omega &= 0 \end{aligned} \tag{34}$$

where  $\mathbf{u} = [w, \theta_x, \theta_y]^T$  and  $\mathbf{v} = [v, \phi_x, \phi_y]^T$  are kinematics state variables and their variations,  $\gamma(\mathbf{u}) = (\frac{\partial w}{\partial x} + \theta_y; \frac{\partial w}{\partial y} - \theta_x)^T$  and  $\gamma(\mathbf{v}) = (\frac{\partial v}{\partial x} + \phi_y; \frac{\partial v}{\partial y} - \phi_x)^T$  are displacement-based shear strains and their variations, while  $\mathbf{q}$  are shear forces. By assuming the shear force is defined independently in each element, we can recover (e.g. see (e.g. see [28])) the variational consistency of the assumed shear strain formulation by enforcing the validity of the variational equation (34) in each element.

Such a mixed variational formulation is the basis for the Discrete Kirchhoff plate element approximation. The DKT plate element provides cubic interpolation of displacement field and quadratic interpolation of rotation field, along

with the zero value of assumed shear strain. Yet, DKT finite element requires only standard degrees of freedom, with  $(w, \theta_x, \theta_y)$  defined at each corner node.

For clarity of how to construct the finite element interpolations of this kind, let us first consider each edge of DKT plate element as a 2-node planar beam FE of length  $L$ . We define the coordinates  $s^B = \xi^B \frac{L}{2} + \frac{L}{2} \in [0, L]$ ,  $\xi^B \in [-1, +1]$ . Along each edge, we choose the following interpolations for displacement (cubic) and rotation (quadratic):

$$w_h^B = \sum_{I=1}^2 w_I N_I^B + \sum_{I=3}^4 w_I N_I^B, \quad \theta_h^B = \sum_{I=1}^2 \theta_I N_I^B + \theta_3 N_3^B \quad (35)$$

where  $N_I^B$  are hierarchical Lagrangian functions  $N_1^B = (1 - \xi^B)/2$ ,  $N_2^B = (1 + \xi^B)/2$ ,  $N_3^B = (1 - (\xi^B)^2)$ ,  $N_4^B = \xi^B(1 - (\xi^B)^2)$ . At the final stage, only two nodal displacements,  $w_1, w_2$ , and two nodal rotations,  $\theta_1, \theta_2$ , will remain as acceptable parameters. The other parameters in (35) are condensed out by enforcing the normality hypothesis of the Kirchhoff theory, and by setting the constant, the linear, and the quadratic terms in  $\frac{\partial w_h^B}{\partial s^B} - \theta_h^B = 0$  to zero; this results with:

$$w_3 = \frac{L}{8}(\theta_1 - \theta_2), \quad w_4 = \frac{L}{4}\left(\frac{w_2 - w_1}{L} - \frac{1}{2}(\theta_1 + \theta_2)\right), \quad \theta_3 = \frac{6}{L}w_4 \quad (36)$$

By replacing (36) into (35), we finally recover a four-parameter interpolation along  $\xi^B$ . Hence, with this interpolation the DKT will have the zero transverse shear imposed along each edge, which for assumed strain interpolation (see [28]) further implies zero shear strains everywhere within the element domain. This result is directly applicable to the DKT element by recognizing that  $\theta_h^B = \mathbf{n}^T \boldsymbol{\theta}_{h,e} = \theta_{n,h,e}$  and that the Kirchhoff normality constraint implies  $\frac{\partial w_{h,e}}{\partial s} - \theta_{n,h,e} = 0$  for each edge of element  $e$ . Thus, we obtain the following DKT approximations of displacement and rotations represented by the sum of nodal,  $I = 1, 2, 3$ , and edge contributions,  $IJ = 12, 23, 31$

$$w_{h|e} = w_{h,e} = \sum_{I=1}^3 w_I N_I + \sum_{IJ} (w_{3,IJ} N_{IJ} + w_{4,IJ} M_{IJ}) \quad (37)$$

$$\boldsymbol{\theta}_{h|e} = \boldsymbol{\theta}_{h,e} = \sum_{I=1}^3 \boldsymbol{\theta}_I N_I + \sum_{IJ} \boldsymbol{\theta}_{3,IJ} N_{IJ}$$

Here,  $w_{3,IJ}$ ,  $w_{4,IJ}$  and  $\boldsymbol{\theta}_{3,IJ}$  are in analogy with parameters in (36)

$$w_{3,IJ} = \frac{L_{IJ}}{8} \mathbf{n}_{IJ}^T (\boldsymbol{\theta}_I - \boldsymbol{\theta}_J), \quad w_{4,IJ} = \frac{L_{IJ}}{4} \left( \frac{w_J - w_I}{L_{IJ}} - \frac{1}{2} \mathbf{n}_{IJ}^T (\boldsymbol{\theta}_I + \boldsymbol{\theta}_J) \right)$$

$$\boldsymbol{\theta}_{3,IJ} = \frac{6}{L_{IJ}} w_{4,IJ} \mathbf{n}_{IJ} \quad (38)$$

where  $\mathbf{n}_{IJ} = [n_{x,IJ}, n_{y,IJ}]^T$  is the outward unit normal of edge between nodes  $I$  and  $J$ , and  $L_{IJ}$  is the length of that edge. The functions in (37) may be defined

in area coordinates  $\zeta_I$ , [39], as  $N_I = \zeta_I$ ,  $N_{IJ} = 4\zeta_I\zeta_J$ , and  $M_{IJ} = 4\zeta_I\zeta_J(\zeta_J - \zeta_I)$ . The above DKT interpolations can also be presented in the matrix notation

$$w_{h,e} = \sum_{I=1}^3 \mathbf{N}_{w,I} \mathbf{u}_I, \quad \boldsymbol{\theta}_{h,e} = \sum_{I=1}^3 \mathbf{N}_{\theta,I} \mathbf{u}_I, \quad \boldsymbol{\kappa}_h = \sum_{I=1}^3 \mathbf{B}_{\kappa,I} \mathbf{u}_I \quad (39)$$

where vector  $\mathbf{u}_I = [w_I, \theta_{xI}, \theta_{yI}]^T$  collects the degrees of freedom of node  $I$ . We will also use notation  $\bar{\mathbf{u}}^e = [\mathbf{u}_1^T, \mathbf{u}_2^T, \mathbf{u}_3^T]^T$ . Explicit forms of  $\mathbf{N}_{w,I}$ ,  $\mathbf{N}_{\theta,I}$  and  $\mathbf{B}_{\kappa,I}$  can be obtained from (37), (38) and (2).

By using the so defined DKT interpolations for both trial,  $\mathbf{u}_{h,e} = [w_{h,e}, \boldsymbol{\theta}_{h,e}^T]^T$ , and test functions,  $\mathbf{v}_{h,e} = [v_{h,e}, \boldsymbol{\phi}_{h,e}^T]^T$ , in the weak form (12), we obtain

$$a_e(\mathbf{u}_{h,e}, \mathbf{v}_{h,e}) = \int_{\Omega_{h,e}} \boldsymbol{\kappa}_h^T(\mathbf{v}_{h,e}) \mathbf{m}_h(\mathbf{u}_{h,e}) d\Omega = \sum_{I,J=1}^3 \mathbf{v}_I^T \mathbf{K}_{IJ}^e \mathbf{u}_J \quad (40)$$

$$\mathbf{K}_{IJ}^e = \int_{\Omega_{h,e}} \mathbf{B}_{\kappa,I}^T \mathbf{C}_B \mathbf{B}_{\kappa,J} d\Omega$$

where  $\mathbf{v}_I = [v_I, \phi_{xI}, \phi_{yI}]^T$ , and  $[\mathbf{K}_{IJ}^e]$  is the element stiffness matrix. The element consistent load vector  $\mathbf{f}^e = [\mathbf{f}_I^{e,T}]^T$  follows from

$$l_e(\mathbf{v}_{h,e}) = \int_{\Omega_{h,e}} v_{h,e} f d\Omega + \sum_{\Gamma_{IJ}} \left[ \int_{\Gamma_{IJ}} (v_{h,e} \bar{q}_{ef} + \phi_{s,h,e} \bar{m}_s) ds + [v_{h,e} \bar{m}_n]_I^J \right] =$$

$$= \sum_{I=1}^3 \mathbf{v}_I^T \mathbf{f}_I^e = \sum_{I=1}^3 \mathbf{v}_I^T (\mathbf{f}_{f,I}^e + \mathbf{f}_{t,I}^e + \mathbf{f}_{c,I}^e)$$

where  $\phi_{s,h,e} = \mathbf{s}_{IJ}^T \boldsymbol{\phi}_{h,e}$ ,  $\mathbf{s}_{IJ} = [-n_{y,IJ}, n_{x,IJ}]^T$ , edge  $\Gamma_{IJ} \subset \Gamma_{N,h}$ , and

$$\mathbf{f}_{f,I}^e = \int_{\Omega_{h,e}} f \mathbf{N}_{w,I} d\Omega, \quad \mathbf{f}_{t,I}^e = \sum_{\Gamma_{IJ}} \int_{\Gamma_{IJ}} (\bar{q}_{ef} \mathbf{N}_{w,I} + \bar{m}_s \mathbf{s}_{IJ}^T \mathbf{N}_{\theta,I}) ds$$

$$\mathbf{f}_{c,I}^e = [\bar{m}_n|_{I^+} - \bar{m}_n|_{I^-}, 0, 0]^T, \quad \forall \text{ node } I \in \Gamma_{N,h} \quad (42)$$

The trial and the test spaces for a plate problem, discretized by the DKT finite element, can be written as:

$$\mathbf{V}_h^{DKT} = \left\{ \begin{array}{l} w_h \in \mathcal{U} \mid w_{h|e} \in P_3(e) \quad \forall e \in \mathcal{C}_h \\ \boldsymbol{\theta}_h \in \mathbf{U} \mid \boldsymbol{\theta}_{h|e} \in [P_2(e)]^2 \quad \forall e \in \mathcal{C}_h \\ \mathbf{n}_{IJ}^T \left( \boldsymbol{\nabla}^K w_{h|e} - \boldsymbol{\theta}_{h|e} \right) |_{\Gamma_{IJ}} = 0 \quad \forall \Gamma_{IJ} \in e \wedge \forall e \in \mathcal{C}_h \end{array} \right\} \quad (43)$$

$$\mathbf{V}_{0,h}^{DKT} = \left\{ \begin{array}{l} v_h \in \mathcal{U}_0 \mid v_{h|e} \in P_3(e) \quad \forall e \in \mathcal{C}_h \\ \boldsymbol{\phi}_h \in \mathbf{U}_0 \mid \boldsymbol{\phi}_{h|e} \in [P_2(e)]^2 \quad \forall e \in \mathcal{C}_h \\ \mathbf{n}_{IJ}^T \left( \boldsymbol{\nabla}^K v_{h|e} - \boldsymbol{\phi}_{h|e} \right) |_{\Gamma_{IJ}} = 0 \quad \forall \Gamma_{IJ} \in e \wedge \forall e \in \mathcal{C}_h \end{array} \right\} \quad (44)$$

where  $P_3(e)$  and  $P_2(e)$  are the spaces of polynomials of degrees at most 3 and 2, respectively, on triangle  $e$  with edges  $\Gamma_{IJ}$ ,  $IJ = 12, 23, 31$ , and nodes  $I = 1, 2, 3$ . The  $\mathcal{C}_h$  represents the collection of all the elements of the mesh, and

$$\mathcal{U} = \{w \in \mathcal{H}^1(\Omega) \mid w = \bar{w} \text{ on } \Gamma_D\}, \quad \mathbf{U} = \left\{ \boldsymbol{\theta} \in [\mathcal{H}^1(\Omega)]^2 \mid \mathbf{s}^T \boldsymbol{\theta} = \bar{\theta}_s \text{ on } \Gamma_D \right\} \quad (45)$$

$$\mathcal{U}_0 = \{v \in \mathcal{H}^1(\Omega) \mid v = 0 \text{ on } \Gamma_D\}, \quad \mathbf{U}_0 = \left\{ \boldsymbol{\phi} \in [\mathcal{H}^1(\Omega)]^2 \mid \mathbf{s}^T \boldsymbol{\phi} = 0 \text{ on } \Gamma_D \right\} \quad (46)$$

Thus, (18) and (19) are for the DKT replaced with

$$\mathbf{V} = \left\{ \begin{array}{l} w \in \mathcal{H}^1(\Omega) \\ \boldsymbol{\theta} \in [\mathcal{H}^1(\Omega)]^2 \end{array} \mid \text{on } \Gamma_D: w = \bar{w}, \mathbf{s}^T \boldsymbol{\theta} = \theta_s = \bar{\theta}_s \right\} \quad (47)$$

and

$$\mathbf{V}_0 = \left\{ \begin{array}{l} v \in \mathcal{H}^1(\Omega) \\ \boldsymbol{\phi} \in [\mathcal{H}^1(\Omega)]^2 \end{array} \mid \text{on } \Gamma_D: v = 0, \mathbf{s}^T \boldsymbol{\phi} = \phi_s = 0 \right\} \quad (48)$$

## 4 Error estimates for Kirchhoff plate elements based upon equilibrated boundary stress resultants

In this section, we define the discretization error and present the computational procedure based upon the equilibrated element boundary stress resultants (EqR), which can be used for any Kirchhoff plate element. The procedure follows the path proposed earlier for classical elasticity problems in [29] or [36].

### 4.1 Global versus local residuals and equilibrated edge tractions

The discretization error is a continuous field defined as the difference between the exact solution  $\mathbf{u}$  and the FE solution  $\mathbf{u}_h$ :

$$\mathbf{e} = \mathbf{u} - \mathbf{u}_h \quad (49)$$

Given that both exact and FE solutions satisfy the weak form of plate equilibrium equations, by linearity of linear and bilinear forms we can easily show the orthogonality of the true error with respect to any test function chosen in discrete approximation space:

$$a(\mathbf{e}, \mathbf{v}_h) = 0 ; \quad \forall \mathbf{v}_h \in \mathbf{V}_{0,h} \subset \mathbf{V}_0 \quad (50)$$

This confirms the best approximation properties (e.g. [39] or [27]), which implies that the finite element methods delivers the best approximate solution in terms of the energy norm, defined by the corresponding bilinear form.

In order to quantify the error we would need to provide the exact solution, which is not available, in general. Thus, the main task reduces to providing instead a sufficient quality replacement of the exact solution, or rather its variation  $\mathbf{v} \in \mathbf{V}_0$ . Given such a replacement, we can define the corresponding error estimates in terms of the global residual equation:

$$\begin{aligned} a(\mathbf{e}, \mathbf{v}) &:= a(\mathbf{u}, \mathbf{v}) - a(\mathbf{u}_h, \mathbf{v}) \\ &= l(\mathbf{v}) - a(\mathbf{u}_h, \mathbf{v}) ; \quad \forall \mathbf{v} \in \mathbf{V}_0 \end{aligned} \quad (51)$$

The computational effort can be significantly reduced if the global residual in (51) is decomposed into contributions from all individual elements of a particular finite element mesh

$$a(\mathbf{e}, \mathbf{v}) = \sum_e [g_e(\mathbf{v}_e) - a_e(\mathbf{u}_{h,e}, \mathbf{v}_e)] + \sum_e \left[ \sum_{\Gamma} \int_{\Gamma} \mathbf{v}_e^T \mathbf{t}_{e,\Gamma} ds \right] \quad \forall \mathbf{v}, \mathbf{v}_e \in \mathbf{V}_0 \quad (52)$$

where  $g_e(\mathbf{v}_e) = \int_{\Omega_{h,e}} v f d\Omega$  and  $\mathbf{t}_{e,\Gamma}$  are the element boundary tractions on each edge  $\Gamma$  in a particular finite element  $e$ . We will use the notation  $\mathbf{t}_{e,\Gamma} = [q_{ef,\Gamma}, m_{s,\Gamma}, m_{n,\Gamma}]^T$ , where  $m_{s,\Gamma} = -m_{nn}|_{\Gamma}$  and  $m_{n,\Gamma} = m_{ns}|_{\Gamma}$ . Since the sum of local residuals in (52) should match the global residual in (51), the total virtual work of element boundary traction forces over all edges must remain equal to zero. Given continuity of test functions across any edge, this further implies that the element boundary tractions must remain continuous across the interior edge between two adjacent elements:

$$\mathbf{t}_{e,\Gamma} + \mathbf{t}_{e',\Gamma} = \mathbf{0} \quad \text{for } e \text{ and } e' \text{ sharing edge } \Gamma \quad (53)$$

The enforcement of condition in (53) above requires the special procedure, which is discussed in subsequent section for DKT plate element. Note that the continuity requirement concerns the moments  $m_{nn}$  and  $m_{ns}$ , or more precisely, only corner nodal moments  $m_{ns}$  and the effective shear force  $q_{ef}$  across all the interior edges. This implies, that the moment  $m_{ss}$ , and the shear force  $q_n$  need not be continuous across the interior edges.

Given such choice of element boundary tractions, we can reduce the computation of discretization error  $\boldsymbol{\vartheta}_e \in \mathbf{V}$  in (51) to local (element-wise) residual computations to be carried out independently in each element  $e$

$$a_e(\boldsymbol{\vartheta}_e, \mathbf{v}_e) = g_e(\mathbf{v}_e) - a_e(\mathbf{u}_{h,e}, \mathbf{v}_e) + \sum_{\Gamma} \int_{\Gamma} \mathbf{v}_e^T \mathbf{t}_{e,\Gamma} ds \quad \forall \mathbf{v}_e \in \mathbf{V} \quad (54)$$

We note that any element edge placed on Dirichlet boundary  $\Gamma \subset \Gamma_{D,h}$  is also considered as an interior edge, where we need to compute the equilibrated element boundary tractions. Only the element edges placed on Neumann boundary  $\Gamma \subset \Gamma_{N,h}$  are left out of this computations, and the corresponding values of element boundary tractions are set equal to the imposed traction vales:

$$\mathbf{t}_{e,\Gamma} = [\bar{q}_{ef}, \bar{m}_s, \bar{m}_n]^T \quad \text{for } \Gamma \subset \Gamma_{N,h} \quad (55)$$



This condition should ensure the accuracy of the computed error with respect to boundary conditions.

Another condition that must be imposed upon the element boundary tractions  $\mathbf{t}_{e,\Gamma}$  concerns the element equilibrium. In other words, for  $\mathbf{v}_e = [1, x, y]^T$ , the edge traction forces should exactly equilibrate the applied external loading. For  $\mathbf{v}_e = \mathbf{v}_{h,e}$ , the Galerkin orthogonality is recovered on the left hand side in (54), with  $a_e(\boldsymbol{\vartheta}_e, \mathbf{v}_{h,e}) = 0$ . This further leads to an additional condition on element boundary traction, which can be written as:

$$\begin{aligned} \sum_{\Gamma_{IJ}} \int_{\Gamma_{IJ}} \mathbf{v}_{h,e}^T \mathbf{t}_{e,\Gamma_{IJ}} ds &= a_e(\mathbf{u}_{h,e}, \mathbf{v}_{h,e}) - g_e(\mathbf{v}_{h,e}) \Leftrightarrow \\ \sum_{\Gamma_{IJ}} (\mathbf{v}_I^T \mathbf{r}_{I,\Gamma_{IJ}}^e + \mathbf{v}_J^T \mathbf{r}_{J,\Gamma_{IJ}}^e) &= \sum_L \mathbf{v}_L^T \mathbf{R}_L^e \end{aligned} \quad (56)$$

Here,  $\mathbf{R}_L^e$  denotes the nodal value at the FE node  $L$  of element residual, obtained as  $\mathbf{R}_L^e = \mathbf{K}_{L,J}^e \mathbf{u}_J - \mathbf{f}_{f,L}^e$ , where  $\mathbf{K}_{L,J}^e$  and  $\mathbf{f}_{f,L}^e$  are the stiffness matrix and the external nodal load vector, respectively. The component  $\mathbf{r}_{I,\Gamma_{IJ}}^e$  may be regarded as projection of  $\mathbf{R}_I^e$  onto edge  $\Gamma_{IJ}$  of a particular element  $e$ . Similarly,  $\mathbf{r}_{J,\Gamma_{IJ}}^e$  can be viewed as projection of  $\mathbf{R}_J^e$  onto edge  $\Gamma_{IJ}$  of element  $e$ . The procedure to construct the element boundary tractions satisfying (56), as well as constraints (53) and (55), must be specified for each particular element; in the next section we discuss the specific choice for DKT plate element.

## 4.2 Enhanced test space, local Neumann problem and error estimates

In seeking the error estimate, we can define the error  $\boldsymbol{\vartheta}_e = \tilde{\mathbf{u}}_e - \mathbf{u}_{e,h}$ , where  $\tilde{\mathbf{u}}_e \in \mathbf{V}$  is an enhanced approximation of the exact solution  $\mathbf{u}_e$ ; this allows to restate the result in (54) as:

$$a_e(\tilde{\mathbf{u}}_e, \mathbf{v}_e) = g_e(\mathbf{v}_e) + \sum_{\Gamma} \int_{\Gamma} \mathbf{v}_e^T \mathbf{t}_{e,\Gamma} ds \quad \forall \mathbf{v}_e \in \mathbf{V} \quad (57)$$

One can then solve (57) instead of (54), to obtain an enhanced solution. This is a local (element-wise) Neumann problem. For simple elements, one can provide the analytic solution to this problem. However, for plates elements this can lead to a prohibitive computational cost (e.g. see [10]). A more efficient alternative is to solve this local Neumann problem with higher-order approximation of test space, i.e.  $\mathbf{v}_{h,e} \rightarrow \mathbf{v}_{h^+,e}$ :

$$a_e(\mathbf{u}_{h^+,e}, \mathbf{v}_{h^+,e}) = g_e(\mathbf{v}_{h^+,e}) + \sum_{\Gamma} \int_{\Gamma} \mathbf{v}_{h^+,e}^T \mathbf{t}_{e,\Gamma} ds \quad \forall \mathbf{v}_{h^+,e} \in \mathbf{V}_{h^+} \subset \mathbf{V} \quad (58)$$

The result (58) can be written explicitly as

$$\begin{aligned} \int_{\Omega_{h,e}} \boldsymbol{\kappa}_{h^+}^T(\mathbf{v}_{h^+,e}) \mathbf{m}_{h^+}(\mathbf{u}_{h^+,e}) d\Omega &= \int_{\Omega_{h,e}} v_{h^+} f d\Omega \\ &+ \sum_{\Gamma_{IJ}} \int_{\Gamma_{IJ}} (v_{h^+} q_{ef,\Gamma} + \phi_{s,h^+} m_{s,\Gamma}) ds + [v_{h^+} m_{n,\Gamma}]_I^J \end{aligned} \quad (59)$$

where  $\mathbf{u}_{h^+,e} = [w_{h^+}, \boldsymbol{\theta}_{h^+}^T]^T \in \mathbf{V}_{h^+}$ ,  $\mathbf{v}_{h^+,e} = [v_{h^+}, \boldsymbol{\phi}_{h^+}^T]^T$ , and  $[q_{ef,\Gamma}, m_{s,\Gamma}, m_{n,\Gamma}]^T = [\bar{q}_{ef}, \bar{m}_s, \bar{m}_n]^T$  for  $\Gamma_{IJ} \subset \Gamma_{N,h}$ .

The local Neumann problem in (59) above results with a set of linear algebraic equations to be solved for each single element

$$\mathbf{K}_+^e \bar{\mathbf{u}}_+^e = \mathbf{f}_+^e \quad (60)$$

The main difficulty in solving this system pertains to singularity of the element stiffness matrix  $\mathbf{K}_+^e$ , which occurs due to pure Neumann boundary and presence of rigid body modes. Thus, a special procedure need to be used in order to solve this system of equations. We collect these three rigid body modes of plate finite element into a matrix  $\mathbf{D}$ . Any nodal displacements/rotation vector due to the rigid body motion can be written as  $\bar{\mathbf{u}}_R^e = \mathbf{D}\boldsymbol{\alpha}$ , where  $\boldsymbol{\alpha}$  is rigid body mode amplitudes. The rigid body motion of the plate finite element produces zero force, and thus we can write:  $\mathbf{0} = \mathbf{K}_+^e \bar{\mathbf{u}}_R^e = \mathbf{K}_+^e \mathbf{D}\boldsymbol{\alpha}$ . We can enforce solvability of the system (60) by regularization, where  $\mathbf{K}_+^e + \mathbf{D}\mathbf{D}^T$  is no longer a singular matrix. Hence, we can thus obtain the unique solution

$$(\mathbf{K}_+^e + \mathbf{D}\mathbf{D}^T) \hat{\mathbf{u}}_+^e = \mathbf{f}_+^e \quad (61)$$

The rigid body modes can be purged from the solution  $\hat{\mathbf{u}}_+^e$  to get the final nodal displacements as the solution to local Neumann problem  $\bar{\mathbf{u}}_+^e = \hat{\mathbf{u}}_+^e - \mathbf{D}\mathbf{D}^T \hat{\mathbf{u}}_+^e$ . We note in passing that the bending moments are not affected by the rigid body modes and can be computed either with  $\hat{\mathbf{u}}_+^e$  or  $\bar{\mathbf{u}}_+^e$ .

With enhanced solution  $\bar{\mathbf{u}}_+^e$  in hand, local error estimates can be computed as

$$\boldsymbol{\vartheta}_e = \mathbf{u}_{h^+,e} - \mathbf{u}_{h,e} \quad (62)$$

The corresponding energy norm of the local error indicator can then be readily obtained as

$$\|\mathbf{e}_{h,e}\|_E^2 = \int_{\Omega_{h,e}} [\boldsymbol{\kappa}_{h^+}(\mathbf{u}_{h^+,e}) - \boldsymbol{\kappa}_h(\mathbf{u}_{h,e})]^T \mathbf{C}_B [\boldsymbol{\kappa}_{h^+}(\mathbf{u}_{h^+,e}) - \boldsymbol{\kappa}_h(\mathbf{u}_{h,e})] d\Omega \quad (63)$$

It has been noted (e.g. [36]) that the same results can be obtained directly from local Neumann problem by using the error field as the test function

$$\begin{aligned} \|\mathbf{e}_e\|_E^2 &\equiv a(\mathbf{e}_e, \mathbf{e}) \\ &= l(\mathbf{v} - \mathbf{v}^h) - a(\mathbf{u}_h, \mathbf{v} - \mathbf{v}^h) ; \forall \mathbf{v}^h \in \mathbf{V}_0^h ; \forall \mathbf{v} \in \mathbf{V}_0 \end{aligned} \quad (64)$$

When the computations are performed for each element of the mesh, the upper bound of the corresponding global error indicators can be estimated simply by using the Cauchy-Schwarz inequality

$$\|\mathbf{e}\|_E^2 \leq \|\mathbf{e}_h\|_E^2 = \sum_e \|\mathbf{e}_{h,e}\|_E^2 \quad (65)$$

## 5 Implementation of equilibrated element boundary traction method for DKT plate element

The equilibrated element boundary resultants method, is outline in previous section 4 for any Kirchhoff plate element. We will provide in this section the implementation details that pertain to the DKT plate element.

### 5.1 Element boundary stress resultants

To find the relationship between the equilibrated tractions  $\mathbf{t}_{e,\Gamma_{IJ}}$  and the nodal edge projections  $\mathbf{r}_{I,\Gamma_{IJ}}^e$  and  $\mathbf{r}_{J,\Gamma_{IJ}}^e$ , the first part of eq. (56) is used

$$\int_{\Gamma_{IJ}} \mathbf{v}_{h,e}^T \mathbf{t}_{e,\Gamma_{IJ}} ds = (\mathbf{v}_I^T \mathbf{r}_{I,\Gamma_{IJ}}^e + \mathbf{v}_J^T \mathbf{r}_{J,\Gamma_{IJ}}^e) \quad (66)$$

For DKT plate element, (66) above can be written explicitly as

$$\int_{\Gamma_{IJ}} (v_h q_{ef,\Gamma_{IJ}} + \mathbf{s}_{IJ}^T \phi_h m_{s,\Gamma_{IJ}}) ds + [v_h m_{n,\Gamma_{IJ}}]_I^J = \mathbf{v}_I^T \mathbf{r}_{I,\Gamma_{IJ}}^e + \mathbf{v}_J^T \mathbf{r}_{J,\Gamma_{IJ}}^e \quad (67)$$

where the DKT interpolations of the transverse displacement and the rotations along the edge  $\Gamma_{IJ}$  follow from (37) and (38) as

$$\begin{aligned} v_h &= v_I \varphi_1 + v_J \varphi_2 + \frac{L_{IJ}}{4} \mathbf{n}_{IJ}^T (\phi_I - \phi_J) \varphi_3 - \frac{L_{IJ}}{3} \Delta \phi_{IJ} \varphi_4 \\ \phi_h &= \phi_I \varphi_1 + \phi_J \varphi_2 + 2 \mathbf{n}_{IJ} \Delta \phi_{IJ} \varphi_3 \end{aligned} \quad (68)$$

Here,  $L_{IJ}$  is the length of the edge,  $\mathbf{n}_{IJ} = [n_x, n_y]^T$  is the edge outward normal,  $\mathbf{s}_{IJ} = [-n_y, n_x]^T$ , and  $\Delta \phi_{IJ} = \frac{3}{2L_{IJ}}(v_J - v_I) - \frac{3}{4} \mathbf{n}_{IJ}^T (\phi_I + \phi_J)$ . The shape functions in (67) are:  $\varphi_1 = (1 - \xi)/2$ ,  $\varphi_2 = (1 + \xi)/2$ ,  $\varphi_3 = (1 - \xi^2)/2$ ,  $\varphi_4 = \xi(1 - \xi^2)/2$ , and  $\xi \in [-1, 1]$ .

In order to evaluate the integral in (67), we need to provide distribution of  $q_{ef,\Gamma_{IJ}}$  and  $m_{s,\Gamma_{IJ}}$  along the edge. The functions  $\psi_I$  and  $\psi_J$  will be used for this purpose, both for  $q_{ef,\Gamma_{IJ}}$  and  $m_{s,\Gamma_{IJ}}$ . By denoting nodal parameters as  $q_{ef,\Gamma_{IJ}}^I$ ,  $q_{ef,\Gamma_{IJ}}^J$ ,  $m_{s,\Gamma_{IJ}}^I$ , and  $m_{s,\Gamma_{IJ}}^J$ , the corresponding interpolations of  $q_{ef,\Gamma_{IJ}}$  and  $m_{s,\Gamma_{IJ}}$  read:

$$q_{ef,\Gamma_{IJ}} = \psi_I q_{ef,\Gamma_{IJ}}^I + \psi_J q_{ef,\Gamma_{IJ}}^J, \quad m_{s,\Gamma_{IJ}} = \psi_I m_{s,\Gamma_{IJ}}^I + \psi_J m_{s,\Gamma_{IJ}}^J \quad (69)$$

For  $m_{n,\Gamma_{IJ}}$ , we will need only the nodal values denoted as  $m_{n,\Gamma_{IJ}}^I$  and  $m_{n,\Gamma_{IJ}}^J$ . The relationship between the nodal parameters of equilibrated tractions and these edge projections follows from (67) in a form of six linear equations

$$\begin{bmatrix} \mathbf{r}_{I,\Gamma_{IJ}}^e \\ \mathbf{r}_{J,\Gamma_{IJ}}^e \end{bmatrix} = \mathbf{A}^q \begin{bmatrix} q_{ef,\Gamma_{IJ}}^I \\ q_{ef,\Gamma_{IJ}}^J \end{bmatrix} + \mathbf{A}^{m_s} \begin{bmatrix} m_{s,\Gamma_{IJ}}^I \\ m_{s,\Gamma_{IJ}}^J \end{bmatrix} + \mathbf{A}^{m_n} \begin{bmatrix} m_{n,\Gamma_{IJ}}^I \\ m_{n,\Gamma_{IJ}}^J \end{bmatrix} \quad (70)$$

where

$$\mathbf{A}^{m_s} = (-n_y \mathbf{A}^{m_x} + n_x \mathbf{A}^{m_y}), \quad \mathbf{A}^{m_n} = \begin{bmatrix} 1 & 0 & 0 & 0 & 0 & 0 \\ 0 & 0 & 0 & 1 & 0 & 0 \end{bmatrix}^T \quad (71)$$

$$\mathbf{A}^k = \begin{bmatrix} \mathbf{a}_{II}^k & \mathbf{a}_{IJ}^k \\ \mathbf{a}_{JI}^k & \mathbf{a}_{JJ}^k \end{bmatrix}, \quad \mathbf{a}_{IJ}^k = \int_{\Gamma_{IJ}} \begin{bmatrix} N_{k,w}^I \\ N_{k,\theta_x}^I \\ N_{k,\theta_y}^I \end{bmatrix} \psi_J \, ds, \quad k \in [q, m_x, m_y]$$

and

$$\begin{aligned} N_{q,w}^I &= \varphi_1 - \varphi_4/2, & N_{q,w}^J &= \varphi_2 + \varphi_4/2 \\ N_{q,\theta_x}^I &= -L_{IJ} n_x (-\varphi_3 + \varphi_4)/4, & N_{q,\theta_x}^J &= -L_{IJ} n_x (\varphi_3 + \varphi_4)/4 \\ N_{q,\theta_y}^I &= -L_{IJ} n_y (-\varphi_3 + \varphi_4)/4, & N_{q,\theta_y}^J &= -L_{IJ} n_y (\varphi_3 + \varphi_4)/4 \end{aligned} \quad (72)$$

$$\begin{aligned} N_{m_x,w}^I &= 3n_x/L_{IJ} \varphi_3, & N_{m_x,w}^J &= -3n_x/L_{IJ} \varphi_3 \\ N_{m_x,\theta_x}^I &= \varphi_1 + 3n_x^2 \varphi_3/2, & N_{m_x,\theta_x}^J &= \varphi_2 + 3n_x^2 \varphi_3/2 \\ N_{m_x,\theta_y}^I &= 3n_x n_y \varphi_3/2, & N_{m_x,\theta_y}^J &= 3n_x n_y \varphi_3/2 \end{aligned} \quad (73)$$

$$\begin{aligned} N_{m_y,w}^I &= 3n_y/L_{IJ} \varphi_3, & N_{m_y,w}^J &= -3n_y/L_{IJ} \varphi_3 \\ N_{m_y,\theta_x}^I &= 3n_x n_y \varphi_3/2, & N_{m_y,\theta_x}^J &= 3n_x n_y \varphi_3/2 \\ N_{m_y,\theta_y}^I &= \varphi_1 + 3n_y^2 \varphi_3/2, & N_{m_y,\theta_y}^J &= \varphi_2 + 3n_y^2 \varphi_3/2 \end{aligned} \quad (74)$$

If one chooses

$$\psi_I = \varphi_1, \quad \psi_J = \varphi_2 \quad (75)$$

the following relationship between the nodal parameters of equilibrated edge tractions and the edge projections is obtained from (70)-(74)

$$\begin{aligned} q_{ef,\Gamma_{IJ}}^I &= -\frac{12}{L_{IJ}^2} \left( n_x (2r_{I,\Gamma_{IJ}}^{m_x} + 3r_{J,\Gamma_{IJ}}^{m_x}) + n_y (2r_{I,\Gamma_{IJ}}^{m_y} + 3r_{J,\Gamma_{IJ}}^{m_y}) \right) \\ m_{s,\Gamma_{IJ}}^I &= \frac{2}{L_{IJ}} (n_y (-2r_{I,\Gamma_{IJ}}^{m_x} + r_{J,\Gamma_{IJ}}^{m_x}) + n_x (2r_{I,\Gamma_{IJ}}^{m_y} - r_{J,\Gamma_{IJ}}^{m_y})) \\ m_{n,\Gamma_{IJ}}^I &= -\frac{1}{L_{IJ}} (n_x (r_{I,\Gamma_{IJ}}^{m_x} + 7r_{J,\Gamma_{IJ}}^{m_x}) + n_y (r_{I,\Gamma_{IJ}}^{m_y} + 7r_{J,\Gamma_{IJ}}^{m_y})) - r_{I,\Gamma_{IJ}}^q \end{aligned} \quad (76)$$

$$\begin{aligned}
q_{ef,\Gamma_{IJ}}^J &= \frac{12}{L_{IJ}^2} \left( n_x(3r_{I,\Gamma_{IJ}}^{m_x} + 2r_{J,\Gamma_{IJ}}^{m_x}) + n_y(3r_{I,\Gamma_{IJ}}^{m_y} + 2r_{J,\Gamma_{IJ}}^{m_y}) \right) \\
m_{s,\Gamma_{IJ}}^J &= \frac{2}{L_{IJ}} (n_y(r_{I,\Gamma_{IJ}}^{m_x} - 2r_{J,\Gamma_{IJ}}^{m_x}) + n_x(-r_{I,\Gamma_{IJ}}^{m_y} + 2r_{J,\Gamma_{IJ}}^{m_y})) \\
m_{n,\Gamma_{IJ}}^J &= -\frac{1}{L_{IJ}} (n_x(7r_{I,\Gamma_{IJ}}^{m_x} + r_{J,\Gamma_{IJ}}^{m_x}) + n_y(7r_{I,\Gamma_{IJ}}^{m_y} + r_{J,\Gamma_{IJ}}^{m_y})) + r_{J,\Gamma_{IJ}}^q
\end{aligned} \tag{77}$$

The notation  $\mathbf{r}_{I,\Gamma_{IJ}}^e = [r_{I,\Gamma_{IJ}}^q, r_{I,\Gamma_{IJ}}^{m_x}, r_{I,\Gamma_{IJ}}^{m_y}]^T$  has been used above. By inserting (76)-(77) into (69), the equilibrated edge tractions  $\mathbf{t}_{e,\Gamma_{IJ}}$  are given as functions of projections  $\mathbf{r}_{I,\Gamma_{IJ}}^e$  and  $\mathbf{r}_{J,\Gamma_{IJ}}^e$  for the chosen interpolation (75).

## 5.2 Construction of equilibrated boundary tractions

We now elaborate on construction of nodal edge projections. Starting from the second part of (56), we obtain the following relation at the FE node  $I$

$$\mathbf{r}_{I,\Gamma_1}^e + \mathbf{r}_{I,\Gamma_2}^e = \mathbf{R}_I^e \tag{78}$$

where  $\Gamma_1$  and  $\Gamma_2$  are two edges of the element  $e$  that meet at the element node  $I$ . Furthermore, the condition (53) requires that edge projections are continuous across the edge; at node  $K$  of the FE mesh, it should hold that

$$\mathbf{r}_{K,\Gamma}^e + \mathbf{r}_{K,\Gamma}^{e'} = \mathbf{0} \quad \text{for } e \text{ and } e' \text{ sharing edge } \Gamma \tag{79}$$

From (78) and (79), one can get a set of linear algebraic equations. Each sets of this kind is formed for the patch of elements attached to a particular node of the FE mesh. For illustration, let us consider a patch of four elements  $\mathcal{P}_K$  that surround node  $K$  of the mesh (see Figure 3). The equations (78) results in this case with

$$\begin{aligned}
\mathbf{R}_K^{e_1} &= r_{K,\Gamma_4}^{e_1} + r_{K,\Gamma_1}^{e_1} \\
\mathbf{R}_K^{e_2} &= r_{K,\Gamma_1}^{e_2} + r_{K,\Gamma_2}^{e_2} \\
\mathbf{R}_K^{e_3} &= r_{K,\Gamma_2}^{e_3} + r_{K,\Gamma_3}^{e_3} \\
\mathbf{R}_K^{e_4} &= r_{K,\Gamma_3}^{e_4} + r_{K,\Gamma_4}^{e_4}
\end{aligned} \tag{80}$$

Moreover, the continuity condition (79) reads

$$\begin{aligned}
r_{K,\Gamma_1}^{e_1} + r_{K,\Gamma_1}^{e_2} &= 0 \\
r_{K,\Gamma_2}^{e_2} + r_{K,\Gamma_2}^{e_3} &= 0 \\
r_{K,\Gamma_3}^{e_3} + r_{K,\Gamma_3}^{e_4} &= 0 \\
r_{K,\Gamma_4}^{e_4} + r_{K,\Gamma_4}^{e_1} &= 0
\end{aligned} \tag{81}$$

The last result can be written as the set of equations with  $\mathbf{r}_{K,\Gamma_k}^{e_k}$  as unknowns

$$\begin{bmatrix} \mathbf{R}_K^{e_1} \\ \mathbf{R}_K^{e_2} \\ \mathbf{R}_K^{e_3} \\ \mathbf{R}_K^{e_4} \end{bmatrix} = \begin{bmatrix} +1 & 0 & 0 & -1 \\ -1 & +1 & 0 & 0 \\ 0 & -1 & +1 & 0 \\ 0 & 0 & -1 & +1 \end{bmatrix} \begin{bmatrix} \mathbf{r}_{K,\Gamma_1}^{e_1} \\ \mathbf{r}_{K,\Gamma_2}^{e_2} \\ \mathbf{r}_{K,\Gamma_3}^{e_3} \\ \mathbf{r}_{K,\Gamma_4}^{e_4} \end{bmatrix} \tag{82}$$

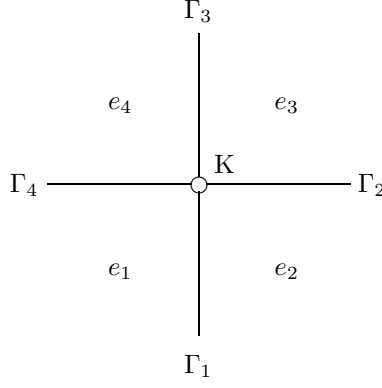


Figure 3: A patch of four elements surrounding node  $K$

The solution to system (82) is not unique. This is the consequence of many possible choices for splitting  $\mathbf{R}_K^e$  into two parts. To obtain the unique solution of (82), some kind of regularization has to be used. The following idea can be exploited for the regularization of system (82): searched projections  $\mathbf{r}_{I,\Gamma}^e$  should be the closest possible in the least squares sense to some known projections  $\tilde{\mathbf{r}}_{I,\Gamma}^e$ . We choose  $\tilde{\mathbf{r}}_{I,\Gamma}^e$  satisfying

$$\int_{\Gamma_{IJ}} \mathbf{v}_{h,e}^T \tilde{\mathbf{t}}_{e,\Gamma_{IJ}} ds = \mathbf{v}_I^T \tilde{\mathbf{r}}_{I,\Gamma_{IJ}}^e + \mathbf{v}_J^T \tilde{\mathbf{r}}_{J,\Gamma_{IJ}}^e \quad (83)$$

where  $\tilde{\mathbf{t}}_{e,\Gamma}$  are assumed to be known edge tractions that are continuous across interior edges, and equal to prescribed loading on plate boundary

$$\tilde{\mathbf{t}}_{e,\Gamma} = [\bar{q}_{ef}, \bar{m}_s, \bar{m}_n]^T \quad \text{for } \Gamma \subset \Gamma_{N,h} \quad (84)$$

By minimizing function, defined over a patch  $\mathcal{P}_K$  that surrounds node  $K$  of the FE mesh

$$J_K(\mathbf{r}_{K,\Gamma_{KI}}^e) = \frac{1}{2} \sum_{e \in \mathcal{P}_K} \sum_{\Gamma_{KI}} (\mathbf{r}_{K,\Gamma_{KI}}^e - \tilde{\mathbf{r}}_{K,\Gamma_{KI}}^e)^2 \mapsto \min \quad (85)$$

the projections  $\mathbf{r}_{K,\Gamma}^e = [r_{K,\Gamma}^q, r_{K,\Gamma}^{m_x}, r_{K,\Gamma}^{m_y}]^T$  can be obtained and further used in (77). Simple averaging can be used to get  $\tilde{\mathbf{t}}_{e,\Gamma}$  in (83)

$$\tilde{\mathbf{t}}_{e,\Gamma} = (\hat{\mathbf{t}}_{e,\Gamma} + \hat{\mathbf{t}}_{e',\Gamma})/2 \quad \text{for } e \text{ and } e' \text{ sharing edge } \Gamma \quad (86)$$

The computation of  $\hat{\mathbf{t}}_{e,\Gamma} = [\hat{q}_{ef,\Gamma}, \hat{m}_{s,\Gamma}, \hat{m}_{n,\Gamma}]^T$  can go as follows. The moments over an entire DKT domain are first obtained as

$$\tilde{\mathbf{m}} = \sum_{I=1}^3 \tilde{\mathbf{m}}_I N_I, \quad \tilde{\mathbf{m}} = [\tilde{m}_{xx}, \tilde{m}_{yy}, \tilde{m}_{xy}]^T \quad (87)$$

where  $N_I$  are Lagrange interpolation functions. Nodal values  $\tilde{\mathbf{m}}_I$  are computed by using the least squares fit of  $\tilde{\mathbf{m}}(\xi_{gp})$  to  $\mathbf{m}_h(\xi_{gp})$ , where  $\xi_{gp}$  are isoparametric coordinates of integration points. At an element edge  $\Gamma$  the transformations (7) are used to get the twisting and the normal moment,  $\tilde{m}_{n,\Gamma} = \tilde{m}_{ns}|_\Gamma$ ,  $\tilde{m}_{s,\Gamma} = -\tilde{m}_{nn}|_\Gamma$ , respectively. The shear force along the same edge is  $\tilde{q}_\Gamma = \tilde{q}_x n_x + \tilde{q}_y n_y$ , where  $\tilde{q}_x = -(\frac{\partial \tilde{m}_{xx}}{\partial x} + \frac{\partial \tilde{m}_{xy}}{\partial y})$  and  $\tilde{q}_y = -(\frac{\partial \tilde{m}_{xy}}{\partial y} + \frac{\partial \tilde{m}_{yy}}{\partial x})$ . Finally, the effective shear force at the edge under consideration is  $\tilde{q}_{ef,\Gamma} = \tilde{q}_\Gamma - \frac{\partial \tilde{m}_n}{\partial s}$ . With these results,  $\hat{\mathbf{t}}_{e,\Gamma}$  in (86) becomes fully defined.

### 5.3 Chosen enhancements of test space

With an already well performing finite element, such as DKT plate, there are not that many optimal solutions for constructing enhanced test space in (58). Some of the existing ones (e.g. [10]) can lead to quite a laborious procedure. Here, we evaluate three simpler solutions for constructing the enhanced space. Two of them are the most straightforward approach by subdividing a single DKT into a number of smaller DKT elements (e.g. [30]), and the third is the one first proposed in terms of the Argyris element.

The simplest enhancement of the DKT test space is subdivision of DKT into 3 triangular elements, as shown in Figure 4. The resulting element, further referred to as the SDKT, has an additional node in the center and 3 additional degrees of freedom. Besides the center node, the SDKT shares all the nodes with the original DKT element. Therefore, the SDKT interpolation will exactly match the DKT interpolation on the edges ( $\mathbf{v}_{h+,e} = \mathbf{v}_{h,e}$  on  $\Gamma$ ). It follows that  $R_I^{e+} = R_I^e$ , which renders the equilibration procedure unnecessary. The procedure using the SDTK to compute error indicators will be called the EqR-SDTK.

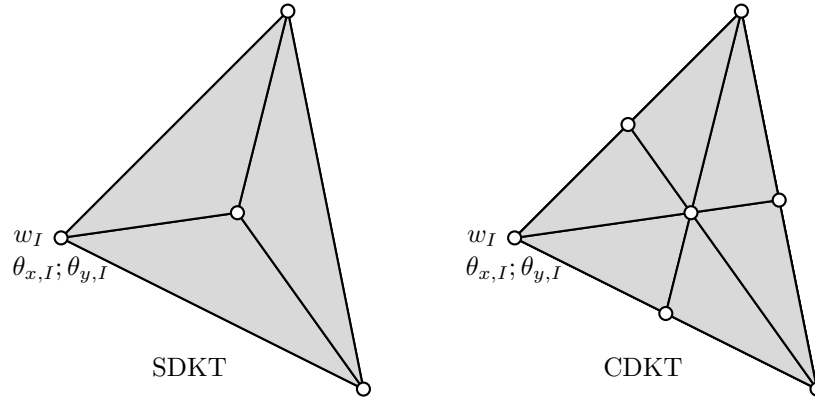


Figure 4: Subdivision schemes for the DKT element

Another subdivision scheme, called the CDKT, uses the SDKT as the starting point. It further subdivides each of 3 triangular elements into 2 by using the symmetry lines between the centre node and the mid-side nodes (see Figure 4). Thus, the CDKT element has in total 7 nodes and 21 degrees of freedom. The procedure that uses the SDKT to compute error indicators will be called the EqR-CDTK.

The final and the best choice for constructing an enhanced test space of the DKT is by using a conforming plate element presented in section 3.1. The element, first proposed in [4] but rather for computing the solution rather than error estimates, will further be called Argyris element. This procedure will be called the EqR-ARGY.

## 6 Numerical examples: error indicators comparison and mesh adaptivity

In this section we carry out a number of numerical simulation in order to provide the illustration of error indicators performance with different enhanced spaces: EqR-SDKT, EqR-CDTK and EqR-ARGY. The results obtained by using the standard smoothing procedure for bending moment computed by DKT plate element over supercovergent patch (e.g. see [39], [35], or [30]) and further referred to as SPR, are also used for comparison.

For any such comparison of different results, we need the exact solution and well defined 'true' error. For the exact solution, we take the strong form solutions, if available (e.g. [37],[14]). Otherwise, the exact solution replacement was obtained by using a very fine mesh with Argyris elements (with curvature values left free). The results are often compared in terms of effectivity index of the proposed error indicator, which is defined as:

$$\Theta = \frac{\|\mathbf{e}_h\|_E}{\|\mathbf{e}\|_E} \quad (88)$$

The second role of numerical examples is to illustrate various aspects of our strategy for mesh adaptivity. For adaptive change of the mesh we will be using the local error indicator. At a single element level, these are denoted as:  $\|\mathbf{e}_{h,e}\|_E = \eta_e^*$ . Their sum over all the elements in the mesh will be denoted as:  $\eta^{*2} = \sum_e \eta_e^{*2}$ . We will also make use of the relative local error indicator  $\eta_{e,r}^*$ , defined as:

$$\eta_{e,r}^* = \frac{\|\mathbf{e}_{h,e}\|_E}{\|\mathbf{n}_{h,e}\|_E}, \quad \|\mathbf{n}_{h,e}\|_E^2 = \int_{\Omega_e} \boldsymbol{\kappa}_h^T \mathbf{m}_h \, ds \quad (89)$$

as well as the relative global error indicator  $\eta_r^*$ , defined as:

$$\eta_r^* = \frac{\|\mathbf{e}_h\|_E}{\|\mathbf{n}_h\|_E}, \quad \|\mathbf{n}_h\|_E^2 = \sum_e \|\mathbf{n}_{h,e}\|_E^2 = \|\mathbf{n}_h\|^2 \quad (90)$$

The main goal of our adaptive strategy is to generate a mesh where the local element error roughly remains constant over the whole domain, i.e. equal in



each element (within the given tolerance) to a prescribed target value. Given such a target value  $\bar{\eta}_e$ , the desired element size  $\bar{h}$  for the error indicator of order  $p$  can be obtained as:

$$\eta_e^* = Ch^p; \quad \bar{\eta}_e = C\bar{h}^p \quad \Rightarrow \quad \bar{h} = h(\bar{\eta}_e/\eta_e^*)^{1/p} \quad (91)$$

where we assumed that a constant  $C$  is independent of element size  $h$ . The computed target values of element size  $\bar{h}$  is stored into a scalar field that is used to guide remeshing in a subsequent step of this adaptive procedure. The software `gmsh` [22] was employed to generate meshes in all different steps.

## 6.1 Clamped square plate under uniform loading

We consider a clamped square plate of side length  $a = 10$  and thickness  $t = 0.01$  under uniform loading  $f = 1$ . The material data is:  $E = 10.92 \cdot 10^{10}$ ,  $\nu = 0.3$ . The closed form analytical expression for the moments, given in [37], is taken as the reference solution (200 terms in series solution were used). The reference solution has no singularities. In Figure 5 we present the curves that show dependency of the global error indicator  $\eta^*$  on the number of elements in a structured mesh. The latter is expressed as  $1/h$ , where  $h^2 = \Omega_h/ne$ , where  $ne$  is the number of elements in the mesh. The EqR-SDKT indicator curve is below the "true error". This indicator thus underestimates the error. The curves of other indicators are larger than the "true error". The effectivity index (Figure 6) is always close to 1.3 for the SPR. The effectivity indices of the EqR-CDKT and the EqR-ARGY are somewhat larger than 1.3. It is important, however, to note the advantage for EqR-ARGY over EqR-CDKT, since both have the same number of 21 unknowns in local Neumann problem.

Another advantage is offered by EqR-ARGY with respect to all other error indicators, if we look at comparison of the relative local error indicators  $\eta_{e,r}^*$ . Namely, as shown in Figure 7, the local error in the corners is quite highly underestimated by both SPR and simple EqR-SDKT error indicators.

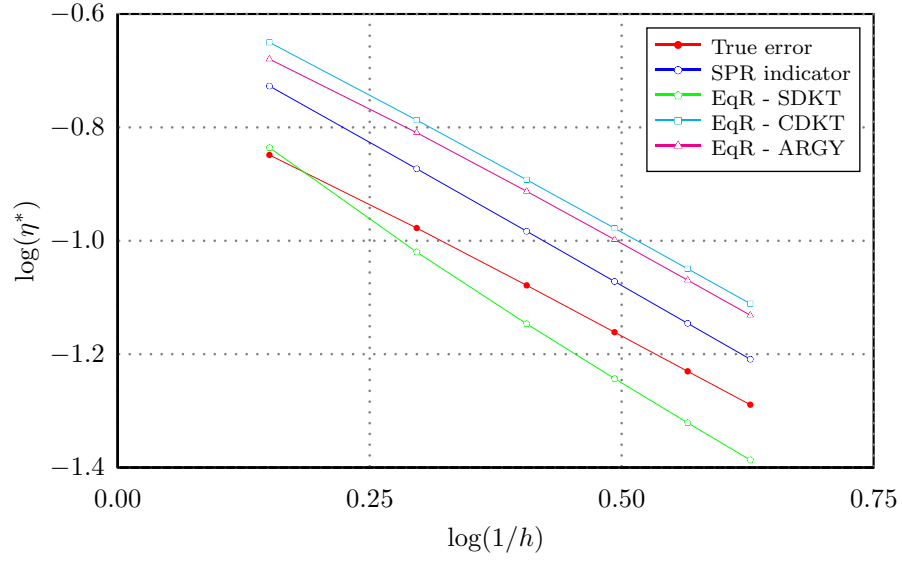


Figure 5: Clamped square plate under uniform loading - global energy error indicator

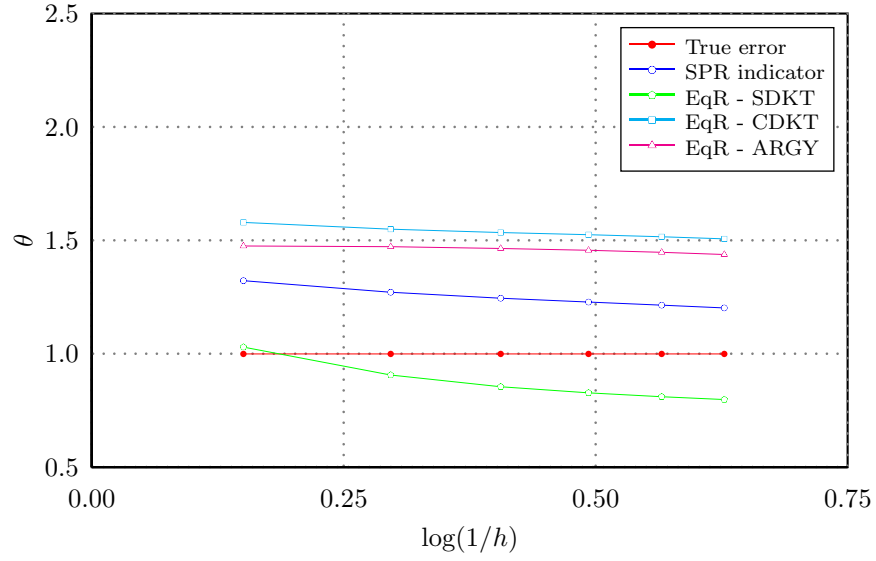


Figure 6: Clamped square plate under uniform loading - effectivity index for the global energy error indicator

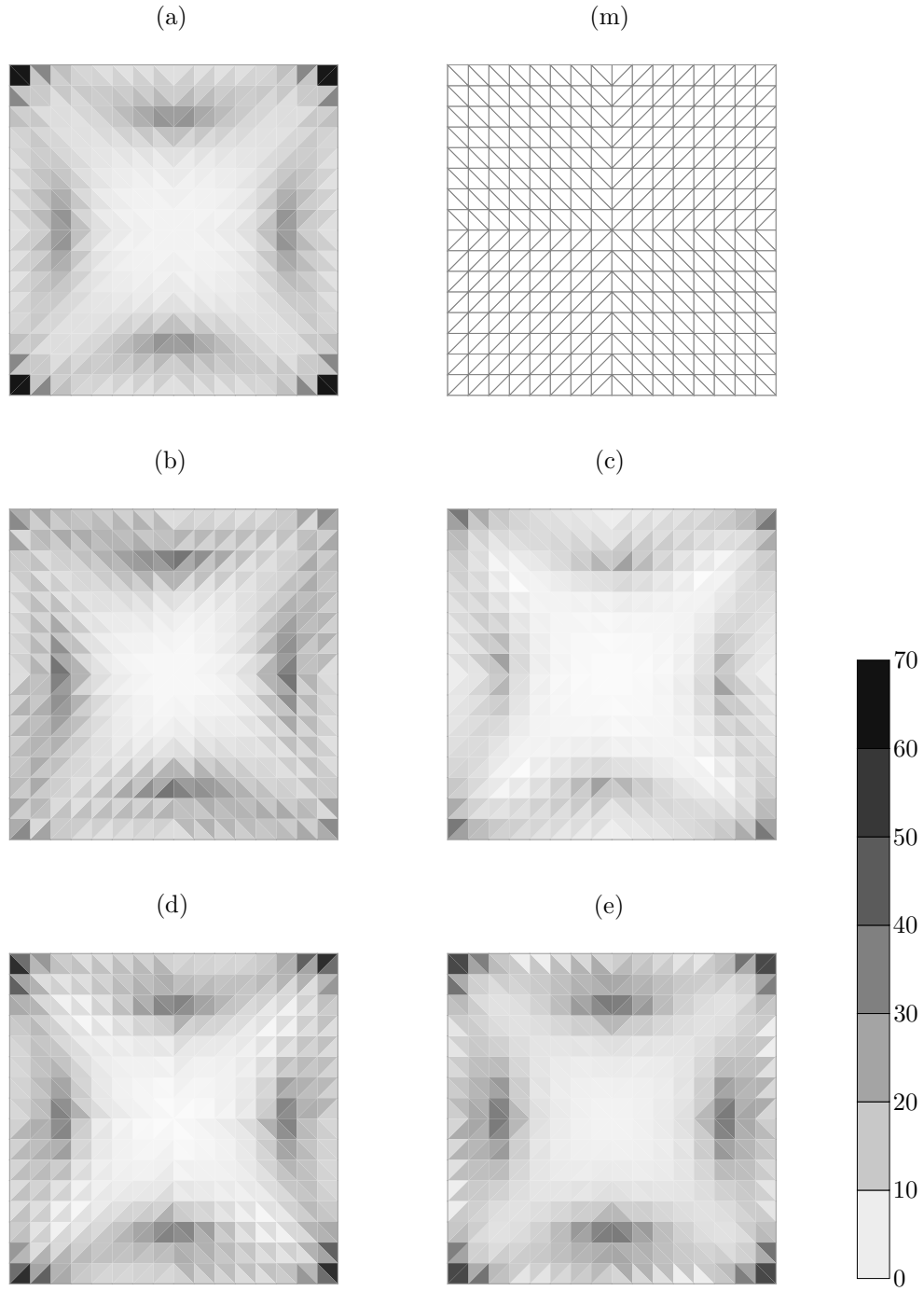


Figure 7: **Clamped square plate under uniform loading**  
Comparison of relative local error indicator  $\eta_{e,r}^*$  in [%] on the mesh (m):  
(a) True error, (b) SPR, (c) EqR-SDKT, (d) EqR-CDKT, (e) EqR-ARGY

## 6.2 Morley's skew plate under uniform loading

The well-known benchmark of Morley's  $30^\circ$  skew plate [33] is analysed in this example. The chosen values for plate thickness  $t = 1$  and side length  $a = 10$ . The plate is resting on simple supports on all sides, under uniformly distributed loading  $f = 1$ . The linear elastic material properties are: Young's modulus  $E = 10.92$  and Poisson's ratio  $\nu = 0.3$ .

The 'exact' solution provided in [33] and it confirmed by computation with Argyris element on regular mesh of  $100 \times 100$  elements with side  $h = 0.1$ . The solution is characterized by two singularity points for moments at the obtuse corners of the plate. The influence of the singularities spreads strongly influencing the quality of computed results (e.g. see [26]).

In Figure 8, we show the global error indicator  $\eta^*$  versus the number of elements computed with a uniform mesh. We first note that the EqR-SDKT exhibits an erratic behaviour, while SPR underestimates the error. The other two indicators, EqR-ARGY and EqR-CDKT, are rather on the safe side by overestimating the error, with equivalent performance for finer meshes and some advantage for EqR-ARGY for coarse meshes. The convergence is not monotonic. The effectivity index curves are presented in Figure 9.

The comparison of the relative local error indicators, given in Figure 10, clearly shows that the EqR-SDKT is completely incapable of capturing the singularities at the obtuse corners, and even the SPR procedure severely underestimates the error. We can also see in this figure that both EqR-ARGY and EqR-CDKT have no difficulties in capturing the singularities.

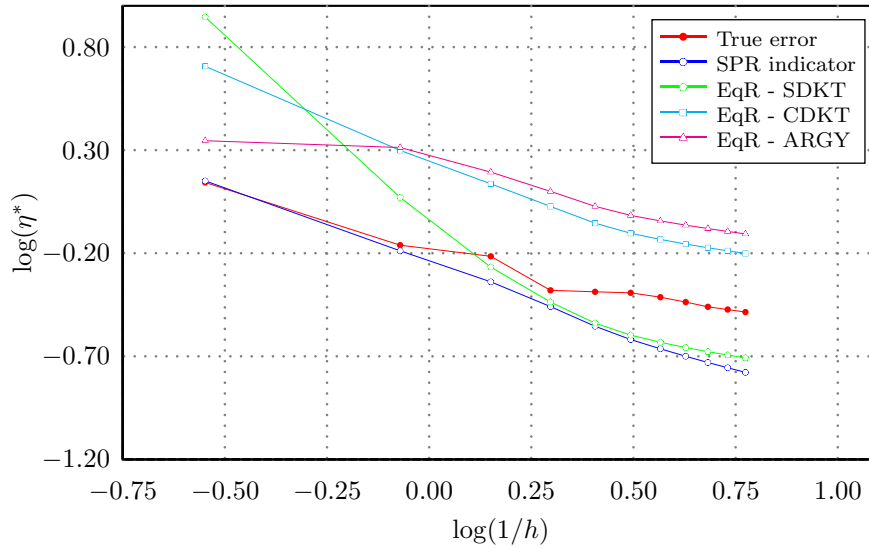


Figure 8: Morley's skew plate under uniform loading - global energy error indicator

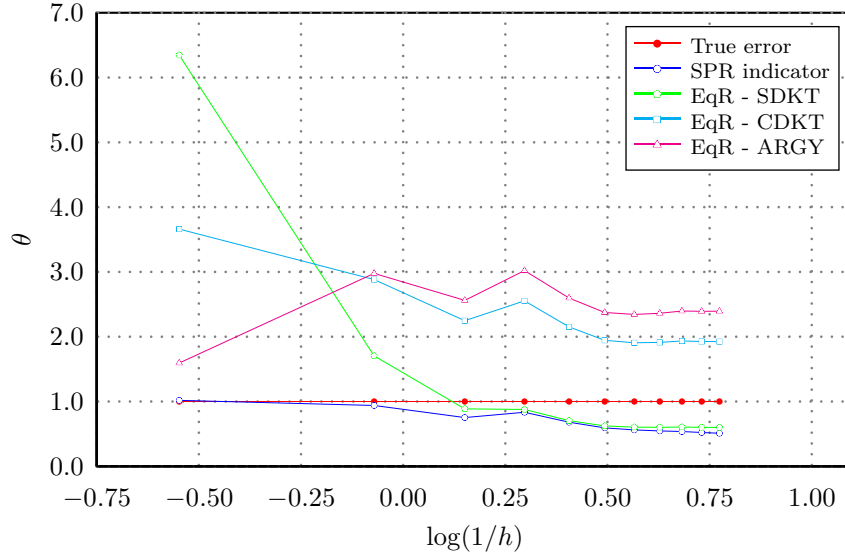


Figure 9: Morley's skew plate under uniform loading - effectivity index for the global energy error indicator

### 6.3 Uniformly loaded clamped square plate

In this example we consider the adaptive mesh refinement in the square plate already considered above. The first FE solution was obtained with a uniform (original) mesh. The problem was then recomputed, with a new mesh generated according to a distribution of the local error indicators  $\eta_e^*$ . It was required that the number of the elements of the new mesh would approximately match the number of the elements of the original mesh. Thus, the average element size was corrected accordingly.

The  $p = 1.1$  was used in (91), which is in accordance with the convergence trends shown in Figure 5 for  $\bar{\eta}_e = 0.05$ . The "true error" was computed by using the reference solution from [37] in the same way as in example 6.1. The results of the computations with the above derived error indicator procedures are summarized in Table 1, which shows new meshes, the distributions of the element error  $\eta_e = \eta_e^*$ , and their histograms. The histograms of the local element error are relatively narrow, except for the original mesh, as expected. The histogram of the second row is not just a single peak. This is due to the limited capability of the mesh generation algorithm, and due to the lack of ability of the error estimate in (91) to take into account the effect of element distortion. The global results do not firmly indicate a superiority of any of the applied procedures, and the mayor difference pertains to the resulting structure of generated meshes. Thus, one has to look again into distribution of the local error indicators clearly shows the difference between the original mesh and the

adapted meshes for different choices of enhanced test space. We note again that EqR-SDKT and SPR cannot fully capture the true need for mesh refinement at the plate corners, which can be obtained correctly with EqR-ARGY and EqR-CDKT.

## 6.4 Uniformly loaded L-shaped plate

In this example, we study an L-shaped plate resting on simple supports under uniform distributed loading  $f = 1$ . We choose the plate thickness  $t = 0.01$  and side length  $a = 10$ . The linear elastic material parameters are: Young's modulus  $E = 10.92 \cdot 10^9$  and Poisson's ratio  $\nu = 0.3$ .

The exact solution exhibits a singularity in stress resultant components at the obtuse corner. The corresponding singularities in  $m_{xx}$  and  $m_{yy}$  are both governed by the term  $r^{\lambda-2}$ , whereas the singularity in  $m_{xy}$  has governing term  $r^{\lambda-3}$ , where  $r$  is the radial distance to the singularity point and  $\lambda$  is the exponent which depends on the opening angle  $\alpha$ , with  $\lambda = \pi/\alpha$  (e.g. see [31]). In our case,  $\alpha = 3\pi/2$ , thus  $\lambda = 2/3$ .

The first solution was obtained on the regular structured mesh shown in Figure 11. The problem was further re-analysed in six iterations, with the remeshing based upon one of three different strategies. (i) The most straightforward mesh refinement strategy was a uniform refinement of a structured mesh. This strategy does not take into account any kind of information about the discretization errors. (ii) Another mesh refinement strategy, that belongs to the same category, was a uniform refinement of an unstructured mesh. For that purpose, the initial structured mesh from Figure 11 was replaced by an unstructured mesh with approximately the same number of elements. (iii) The third strategy is the adaptive meshing based upon different error indicators defined previously. The 'true' error was computed by using the reference solution obtained with a refined mesh of Argyris elements, each with element side  $h = 0.1$ . At each iteration, distribution of error indicator  $\eta_e = \eta_e^*$  was computed. Based on the estimated new element-size density (91), a new mesh was generated with  $p = 1$  and  $\bar{\eta}_e = 0.05$ .

Comparison of the results convergence is shown in Figure 12. The convergence of the adaptive meshing (iii) is considerably faster than uniform mesh refinements (i) and (ii). The difference between applied error indicators in the framework of (iii) disappears after the first two iterations. This is due to the limitation of the minimum allowable element size in the meshing algorithm. If that limitation had not existed, the element size at the singular points would have tend to zero.

Table 2 compares results of different error indicators after the third iteration. The comparison reveals that the distribution of the local error indicator is considerably more uniform for (iii) than for (i), the later shown in the first row. This is precisely one of the primary goals of adaptive meshing, making the local error indicators approximately equal for all elements in the mesh. Another important confirmation of the intrinsic value of mesh refinement strategy is that even though the average of local error indicators is smaller for the uniformly


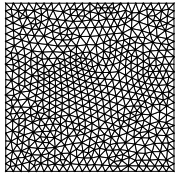
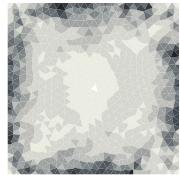
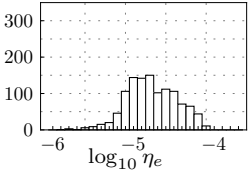
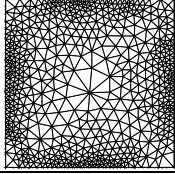
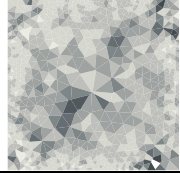
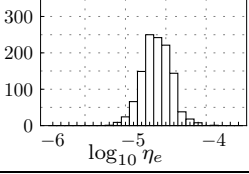
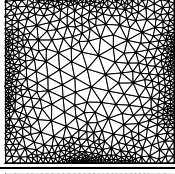
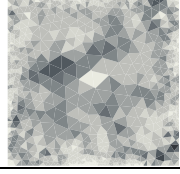
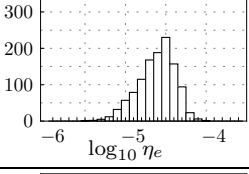
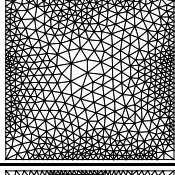
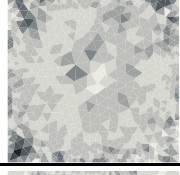
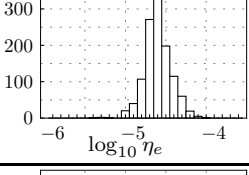
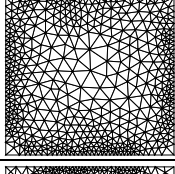
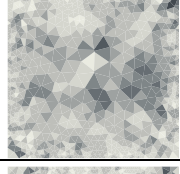
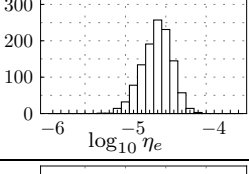
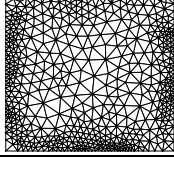
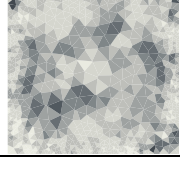
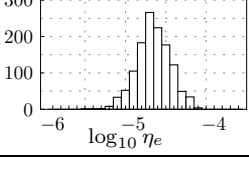
	Mesh	Local element error $\eta_e$ 	Histogram of local element error $\eta_e$
<i>Original mesh</i>  1156 elements, $\eta_r$ : 6.2%			
<i>Mesh based on true error</i>  1171 elements, $\eta_r$ : 5.4%			
<i>Mesh based on SPR</i>  1170 elements, $\eta_r$ : 5.7%			
<i>Mesh based on EqR-SDKT</i>  1168 elements, $\eta_r$ : 5.5%			
<i>Mesh based on EqR-CDKT</i>  1158 elements, $\eta_r$ : 5.4%			
<i>Mesh based on EqR-Argyris</i>  1261 elements, $\eta_r$ : 5.4%			

Table 1: Adaptive meshing of square plate by using different procedures.

refined mesh (see histogram in the first row of Table 2), the total energy norm of the error is still larger (see Figure 12).

## 6.5 Computational cost for used procedures

Here, we briefly summarize the important information regarding the computational cost for the proposed the EqR mesh adaptivity procedures of the comparison strategy SPR. The computational effort of the SPR is proportional to the total number of nodes  $n_{nodes}$  in a mesh, since it relies on the patch-wise computations for each node. The number of computational operations for the SPR  $N_{SPR}$  is thus equal to:

$$N_{SPR} = C_{SPR} n_{nodes} \quad (92)$$

The proportionality constant  $C_{SPR}$  is directly related to the order of local interpolation and the number of element superconvergent points. When linear interpolation is used, and 3 superconvergent points are taken into account for each element,  $C_{SPR} \approx 10$ .

The computational cost for EqR procedure pertains to its three main steps: (i) equilibration of nodal element residuals, (ii) computation of edge generalized forces from the edge projections, and (iii) construction and solution of local (element) problems. The total number of operations is:

$$N_{EqR} = C_{(i)} n_{nodes} + C_{(ii)} n_{edges} + C_{(iii)} n_{elements}$$

where  $C_{(i)}$ ,  $C_{(ii)}$  and  $C_{(iii)}$  are constants that are independent of  $n_{nodes}$  (they are, however, proportional to the number of element degrees of freedom  $n_{dof}$ ). The number of elements, and total number of element edges is denoted by  $n_{elements}$  and  $n_{edges}$ , respectively. Both are directly proportional to  $n_{nodes}$

$$n_{elements} = K_1 n_{nodes}, \quad n_{edges} = K_2 n_{elements} = K_2 K_1 n_{nodes} = K_3 n_{nodes}$$

The above constants are approximately  $K_1 \approx 2$ , and  $K_2 \approx 3/2$  for the triangular unstructured mesh. The computational effort of the EqR method can thus be estimated as

$$N_{EqR} = C_{EqR} n_{nodes}, \quad C_{EqR} = n_{dof} (c_{(i)} + c_{(ii)} K_2 + c_{(iii)} K_1 K_2) \quad (93)$$

The constant  $c_{(i)}$  is proportional to the number of edges meeting at each node, while constants  $c_{(ii)}$  and  $c_{(iii)}$  are proportional to the  $\log(n_{dof})$ . In the case of unstructured triangular mesh and the DKT element,  $C_{EqR} \approx 50$ .

From (92) and (93), we can see that the computational effort for both the SPR and the EqR is finally proportional to the number of nodes  $n_{nodes}$ . The ratio  $C_{EqR}/C_{SPR}$  defines the computational effort of the EqR method compared to the SPR. For the DKT elements, the computational effort of the EqR is approximately 5 times higher than the computational effort of the SPR.

**Acknowledgements:** This work was supported by French-Slovenian collaborative program, Slovenian Ministry of Science and French Ministry of Foreign Affairs. This support is gratefully acknowledged. We would also like to thank to Prof. Pierre Ladevèze for a number of helpful comments.



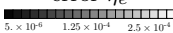
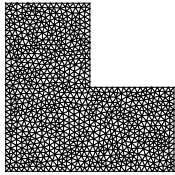
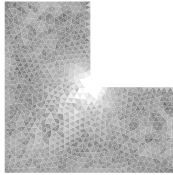
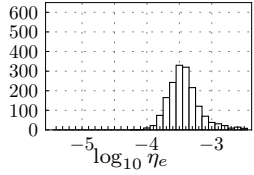
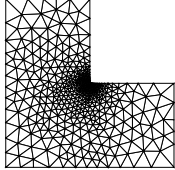
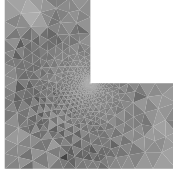
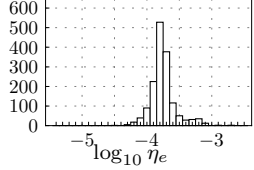
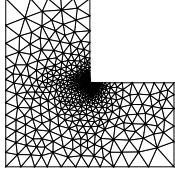
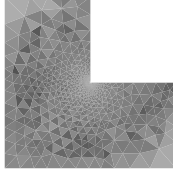
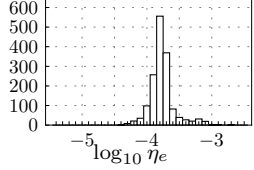
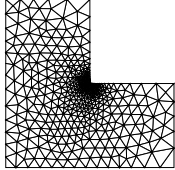
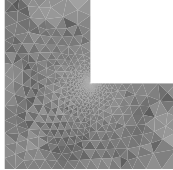
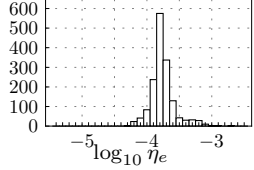
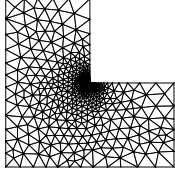
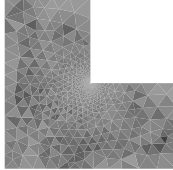
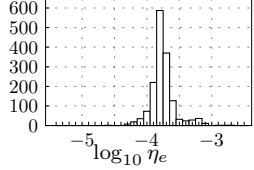
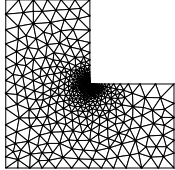
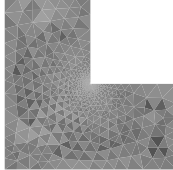
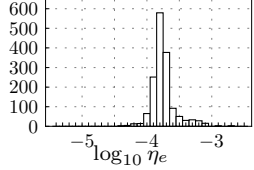
	Mesh after 3rd refinement step	Local element error $\eta_e$ 	Histogram of local element error $\eta_e$
<i>Uniformly refined mesh</i>			
1716 elements, $\eta_r$ : 18.1%			
<i>Mesh based on true error</i>			
1559 elements, $\eta_r$ : 5.8%			
<i>Mesh based on SPR</i>			
1568 elements, $\eta_r$ : 6.5%			
<i>Mesh based on EqR-SDKT</i>			
1575 elements, $\eta_r$ : 6.0%			
<i>Mesh based on EqR-CDKT</i>			
1574 elements, $\eta_r$ : 5.9%			
<i>Mesh based on EqR-Argyris</i>			
1557 elements, $\eta_r$ : 5.6%			

Table 2: Adaptive meshing of L shaped plate by using different procedures.

## 7 Conclusions

The main thrust of this work is directed towards a question of the choice of adaptive mesh refinement for the Discrete Kirchhoff Triangular (DKT) plate bending finite element. The pertinent error indicators are constructed by using the equilibrated residual method adapted to suit this particular element, which is one of the favourite choice in engineering analysis of plates. Therefore, we believe that the proposed error indicators will be of great practical interest.

Among different possibilities for constructing an enhanced test space needed for equilibrated element residual method (e.g. by subdivision of DKT element), the most efficient was proved to be the one constructed by using the Argyris plate element. The Argyris element discrete approximation is the complete fifth order polynomial, which can provide the corresponding enhancement of the third order polynomial used by DKT plate element for transverse displacement field. The main difficulty for using the Argyris plate element in engineering analysis, concerning imposed nodal values of curvatures, does not occur when solving the local Neumann problem for constructing the corresponding enhanced space by the Argyris element.

The superiority of the Argyris element based construction of error indicators by equilibrated element residual method was also shown with respect to the classical technique of superconvergent patch recovery, especially in terms of its to properly provide the local error indicators. This improved result quality does impose somewhat higher computational cost than the one typical of superconvergent patch recovery. Moreover, the computational cost of the proposed error indicator solving 21 equations in each local Neumann problem is still quite acceptable (even lower than some previous proposals; e.g. [10]).

## References

- [1] M. Ainsworth and J.T. Oden. A unified approach to a posteriori error estimation using element residual methods. *Numerische Mathematik*, 65(1):23–50, 1993.
- [2] M. Ainsworth and J.T. Oden. *A posteriori error estimation in finite element analysis*. Wiley, 2000.
- [3] S.M. Allesandrini, D.N. Arnold, R.S. Falk, and A.L. Madureira. Derivation and justification of plate models by variational methods. *CRM/AMS Proceedings 'Plates and Shells' (ed. M. Fortin)*, pages 1–21, 1999.
- [4] J.H. Argyris, I. Fried, and D.W. Scharpf. The TUBA family of plate elements for the matrix displacement method. *The aeronautical journal of the royal aeronautical society*, 72:701–709, 1968.
- [5] I. Babuska, J. Osborn, and J. Pitkaranta. Analysis of mixed methods using mesh dependent norms. *Mathematics of Computations*, 35(152):1039–1062, 1980.

- [6] I. Babuska and W.C. Rheinboldt. Error estimates for adaptive finite element computations. *SIAM J. Numer. Anal.*, 15:736–754, 1978.
- [7] J.L. Batoz. An explicit formulation for an efficient triangular plate-bending element. *International Journal of Numerical Methods in Engineering*, 18:1077–1089, 1982.
- [8] J.L. Batoz, K.J. Bathe, and L.W. Ho. A study of three-node triangular plate bending elements. *International Journal of Numerical Methods in Engineering*, 15:1771–1812, 1980.
- [9] R. Becher and R. Rannacher. An optimal control approach to a posteriori error estimation in finite element methods. *Acta Numerica*, pages 1–102, 2001.
- [10] C. Benoit, P. Coorevits, and J.P. Pelle. Error estimation for plate structures: Application using the DKT element. *Engineering Computations*, 16(5):584–600, 1999.
- [11] M. Bernadou. *Finite element method for the shell problem*. Wiley, 1996.
- [12] U. Bohinc, A. Ibrahimbegovic, and B. Brank. Model adaptivity for finite element analysis of thin or thick plates based on equilibrated boundary stress resultants. *Engineering Computations*, 26(1/2):69–99, 2009.
- [13] D. Braess, S. Sauter, and C. Schwab. On the justification of plate models. *Journal of Elasticity*, 103:53–71, 2011.
- [14] B. Brank. On boundary layer in the Mindlin plate model: Levy plates. *Thin-walled Structures*, 46(5):451–465, 2008.
- [15] B. Brank, J. Korelc, and A. Ibrahimbegovic. Nonlinear shell problem formulation accounting for through-the-thickness stretching and its finite element implementation. *Computers and Structures*, 80:699–717, 2002.
- [16] F. Brezzi. Nonstandard finite elements for fourth order elliptic problems. in *Energy methods in FE analysis (eds. R. Glowinski, E.Y. Rodin, O.C. Zienkiewicz)*, ch. 10:193–211, 1979.
- [17] U. Brink and E. Stein. A posteriori error estimators in large strain elasticity using equilibrated neumann problems. *Computer Methods in Applied Mechanics and Engineering*, 161:77–101, 1998.
- [18] P.G. Ciarlet. *Basic Error Estimates for Elliptic Problems*. Handbook of Numerical Analysis, vol II, Elsevier, 1991.
- [19] R.W. Clough and C.A. Felippa. A refined quadrilateral element for analysis of plate bending. *Proc. Conf. on Matrix Methods in Structural Mechanics, WPAFB, Ohio*, pages 399–440, 1965.

- [20] R.W. Clough and J.L. Tocher. Finite element stiffness matrices for analysis of plate bending. *Proc. Conf. on Matrix Methods in Structural Mechanics, WPAFB, Ohio*, pages 515–545, 1965.
- [21] L.B. Da Veiga, J. Niranen, and R. Stenberg. A posteriori error analysis for the Morley plate element with general boundary conditions. *Numerische Mathematik*, 106(2):165–179, 2007.
- [22] C. Geuzaine and J.-F. Remacle. Gmsh: a three-dimensional finite element mesh generator with built-in pre- and post-processing facilities. *International Journal for Numerical Methods in Engineering*, 79(11):1309–1331, 2009.
- [23] J. Hu and Z. Shi. A new a posteriori error estimate for the Morley element. *Numerische Mathematik*, 112(1):25–40, 2009.
- [24] T.J.R. Hughes. *The Finite Element Method: Linear Static and Dynamic Finite Element Analysis*. Dover publications, 2000.
- [25] A. Ibrahimbegovic. Plate quadrilateral finite element with incompatible modes. *Communications in Applied Numerical Methods*, 8:497–504, 1992.
- [26] A. Ibrahimbegovic. Quadrilateral finite elements for analysis of thick and thin plates. *Computer Methods in Applied Mechanics and Engineering*, 110:195–209, 1993.
- [27] A. Ibrahimbegovic. *Nonlinear solid mechanics: Theoretical Formulations and Finite element Solution Methods*. Springer, Berlin, 2009.
- [28] A. Ibrahimbegovic and F. Frey. Efficient implementation of stress resultant plasticity in analysis of reissner-mindlin plates. *International Journal for Numerical Methods in Engineering*, 36:303–320, 1993.
- [29] P. Ladevèze and D. Leguillon. Error estimate procedure in the finite element method and applications. *SIAM Journal of Numerical Analysis*, 20(3):485–509, 1983.
- [30] P. Ladevèze and J.P. Pelle. *Mastering Calculations in Linear and Nonlinear Mechanics*. Springer, 2005.
- [31] K.H. Lee, G. T. Lim, and C. M. Wang. Thick levy plates re-visited. *International Journal of Solids and Structures*, 39:127–144, 2002.
- [32] C. Lovadina and R. Stenberg. A posteriori error analysis of the linked interpolation technique for plate bending problems. *SIAM journal on numerical analysis*, 43(5):2227, 2005.
- [33] L.S.D. Morley. *Skew plates and structures*. Pergamon press, 1963.
- [34] J. N. Reddy. *Mechanics of laminated composite plates. Theory and analysis*. CRC press, 1998.

- [35] E. Stein. *Error controled adaptive finite elements in solid mechanics*. Wiley, 2003.
- [36] E. Stein and S. Ohnibus. Anisotropic discretization- and model-error estimation in solid mechanics by local neumann problems. *Computer Methods in Applied Mechanics and Engineering*, 176:363–385, 1999.
- [37] R.L. Taylor and S. Govindjee. Solution of clamped rectangular plate problems. *Report UCB/SEMM-2002/09*, 2002.
- [38] S.M. Yunus, T.P. Pawlak, and M.J. Wheeler. Application of the Zienkiewicz-Zhu error estimator for plate and shell analysis. *International journal for numerical methods in engineering*, 29(6):1281–1298, 1990.
- [39] O.C. Zienkiewicz and R.L. Taylor. *Finite element method*. Elseiver, 2000.
- [40] O.C. Zienkiewicz and J.Z. Zhu. The superconvergent patch recovery and a posteriori error estimates. part 1: The recovery technique. *International Journal of Numerical Methods in Engineering*, 33:1331–1364, 1992.

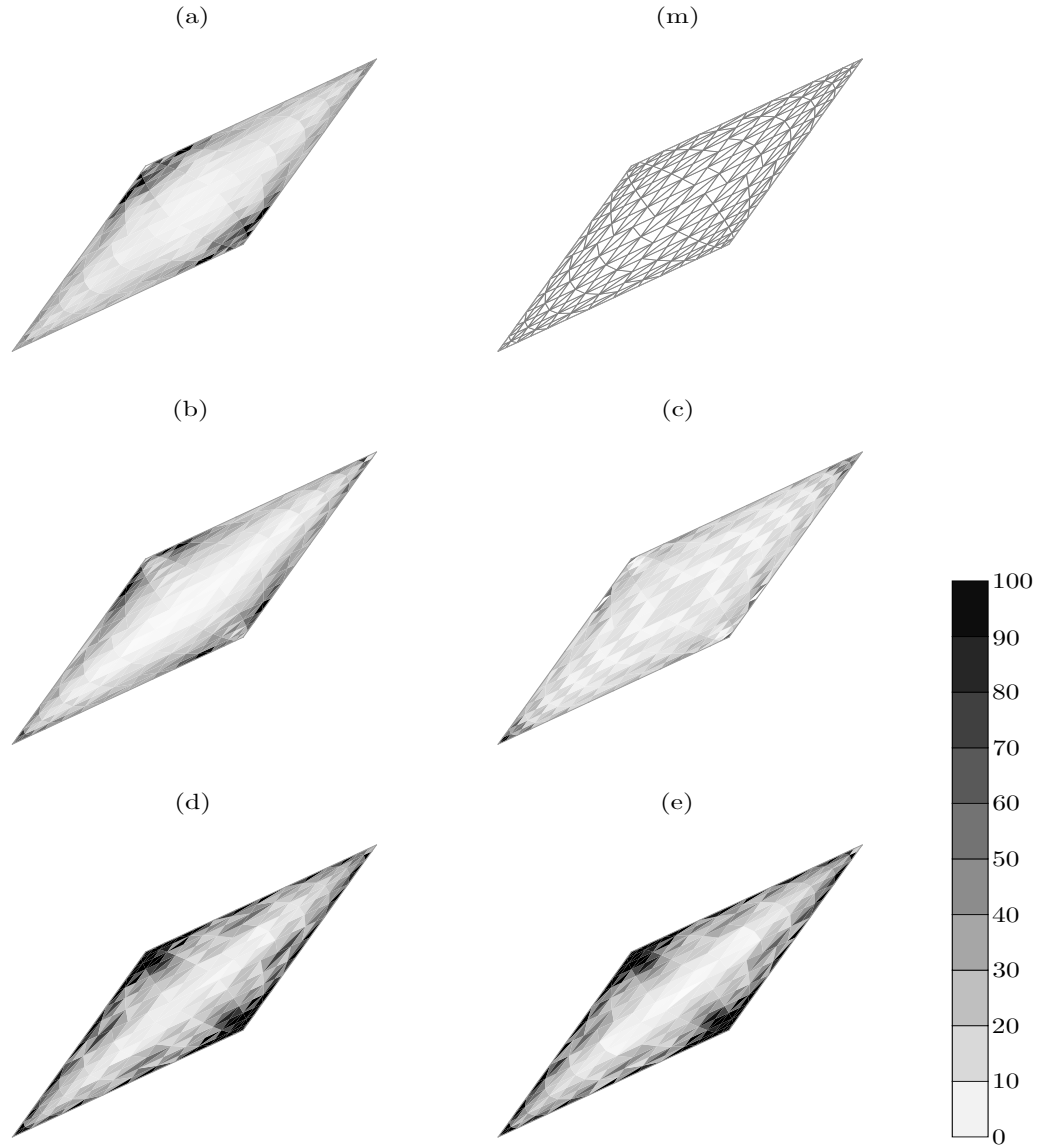


Figure 10: **Morley's skew plate under uniform loading**  
Comparison of relative local error indicators  $\eta_{e,r}^*$  in [%] on the mesh (m):  
(a) True error, (b) SPR, (c) EqR-SDKT, (d) EqR-CDKT, (e) EqR-ARGY

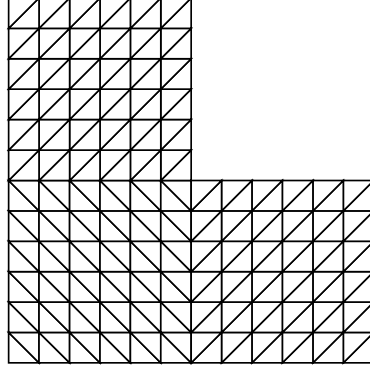


Figure 11: L-shaped plate under uniform loading - initial mesh

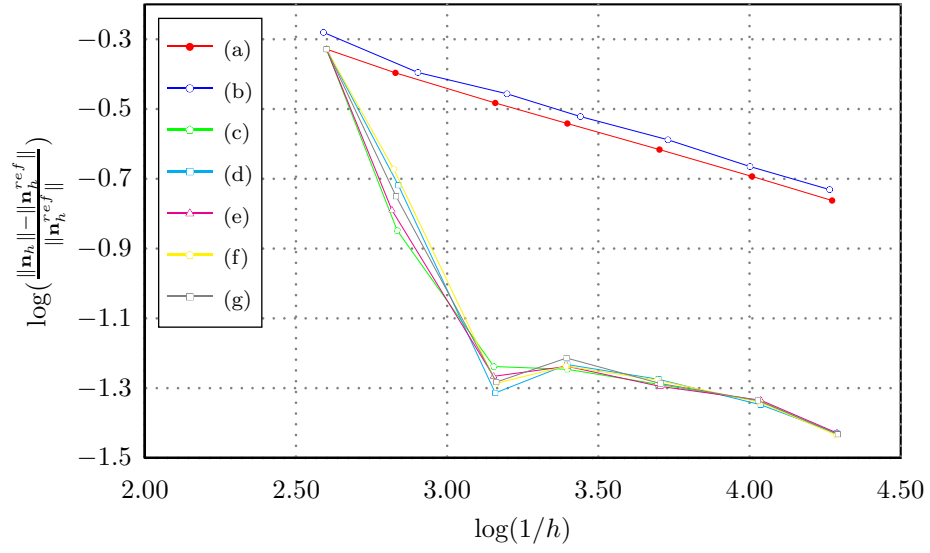


Figure 12: **L-shaped plate under uniform loading:**

Convergence for: (a) Uniform mesh refinement of structured mesh, (b) Uniform mesh refinement of unstructured mesh, (c) Adaptive meshing based on true error, (d) Adaptive meshing based on SPR, (e) Adaptive meshing based on EqR-ARGY, (f) Adaptive meshing based on EqR-SDKT, (g) Adaptive meshing based on EqR-CDKT